CO₂ and CO temporal variability over Mexico City from ground-based total column and surface measurements

Noémie Taquet[1], Wolfgang Stremme[1], María Eugenia González del Castillo[1], Victor Almanza[1], Alejandro Bezanilla[1], Olivier Laurent[2], Carlos Alberti[3], Frank Hase[3], Michel Ramonet[2], Thomas Lauvaux[4], Ke Che[4], Michel Grutter[1]

[1]Instituto de Ciencias de la Atmósfera y Cambio Climático, Universidad Nacional Autónoma de México, México
[2]Laboratoire des Sciences du Climat et de l'Environnement (LSCE), IPSL, CEA-CNRS-UVSQ, Université Paris-Saclay, Gif-sur-Yvette, France
[3]Institute of Meteorology and Climate Research (IMK-ASF), Karlsruhe Institute of Technology (KIT), Karlsruhe, Germany
[4]Groupe de Spectrométrie Moléculaire et Atmosphérique (GSMA), Université de Reims-Champagne Ardenne, UMR CNRS 7331, Reims, France

Correspondence to: Noémie Taquet (noemi.taquet@gmail.com)

Abstract.

Accurate estimates of greenhouse gas emissions and sinks are critical for understanding the carbon cycle and identifying key drivers of anthropogenic climate change. In this study, we investigate the variability of CO and CO_2 concentrations and their ratio over the Mexico City Metropolitan Area (MCMA) from long-term time-resolved columnar measurements at three stations, using solar absorption Fourier transform infrared spectroscopy (FTIR). Using a simple model and the mixed layer height derived from a ceilometer, we determined the CO and CO_2 concentration in the mixed layer from the total column measurements and found good agreement with surface cavity ring-down spectroscopy measurements. In addition, we used the diurnal pattern of CO columnar measurements at specific time intervals to estimate an average growth rate that, when combined with the space-based TROPOMI CO measurements, allowed deriving annual CO and CO_2 MCMA emissions from 2016 to 2021. A decrease of more than 50% of the CO emissions was found during the COVID19 lockdown period with respect to the year 2018. These results demonstrate the feasibility of using long-term EM27/Sun column measurements to monitor the annual variability of anthropogenic CO_2 and CO emissions in Mexico City without recourse to complex transport models. This simple methodology could be adapted to other urban areas if the orography favours low ventilation for several hours per day, which allows that column growth rate to be dominated by emission flux.

1 Introduction

The greenhouse gas (GHG) mitigation strategies implemented in megacities following the 1997 Kyoto Protocol and the 2015 Paris Agreement play a crucial role in the global action plan to mitigate climate change, given that cities are accountable for more than 70% of the global anthropogenic emissions (Duren and Miller, 2012). With the recent progress in space-based and ground-based remote GHG measurements in terms of accuracy, spatial coverage, resolution and temporal frequency, GHG emissions can increasingly be constrained by comparing bottom-up and top-down estimates. Top-down approaches are generally based on ground- or space-based atmospheric measurements coupled with inverse modelling, using 3D-Eulerian (i.e: WRF-Chem) or Lagrangian and hybrid (i.e: X-STILT, Hysplit) approaches (Wu et al., 2018, Che et al., 2022; Lian et al., 2023).

44   The quantification of anthropogenic CO_2 enhancements from cities using satellite data e.g: GOSAT (Wang et al.,
45   2019), OCO-2 (Ye et al., 2020) or TanSat (Liu et al., 2018) is still challenging due to the sparsity of the
46   observations, the low signal from the anthropogenic contribution compared to the background levels and
47   biogenic contribution, and some inconveniences inherent to space-measurements such as the non-negligible
48   aerosol effects (Wang et al., 2020 and references therein). Some studies have estimated the urban enhancements
49   of anthropogenic CO_2 concentrations along with CO and NO_2 from satellite measurements, as these air
50   pollutants can serve as tracers of anthropogenic CO_2 (Silva et al.,2013; Park et al., 2021 and references therein).
51   The CO/CO_2 ratio is often used to determine the combustion efficiency of the cities (Park et al., 2021 and
52   references therein). With the development of a new generation of space-based observatories, such as Sentinel-5P
53   and OCO-2,3, the evolution of GHGs at the city scale can now be characterised with a finer temporal and spatial
54   resolution (Kiel et al., 2021) but more validation efforts are needed. As inverse modelling is likely undermined
55   by the approximations used for defining the emission patterns, transport processes and meteorology, top-down
56   approaches may lead to discrepancies in emissions estimates, in particular in sites with complex orography.

57   Ground-based total column FTIR instruments provide valuable long-time concentration measurements
58   of GHG and pollutant reactive species, as well as anthropogenic tracers, constituting a key element to validate
59   regional and local inventories. Some studies reported estimates of CO_2 and CH_4 emissions from large urban
60   areas (Babenhauserheide et al., 2018 in Tokyo; Hedelius et al., 2018 in the California Southern Coast Air Basin
61   California megacity), using data from high-resolution FTIR instruments (i.e: Bruker IFS120/5HR) contributing
62   to the Total Column Carbon Observing Network (TCCON). Nevertheless, only a few TCCON stations are
63   located in urban areas (Toon et al., 2009; Chevallier et al., 2011; Sussman et al., 2020). The development of the
64   COllaborative Carbon Column Observing Network (COCCON, Frey et al., 2019), using a new generation of
65   portable low spectral resolution FTIR spectrometers (EM27/SUN, Gisi et al., 2012; Hase et al., 2016) able to
66   simultaneously measure the CO_2, CO, H_2O and CH_4 average total columns with a similar quality as TCCON, has
67   considerably densified the number of measurements in urban environments. Some studies reported emission
68   estimates for big cities by means of the deployment of several EM27/SUN instruments at strategic sites
69   throughout the cities (Hase et al., 2015 and Zhao et. al., 2019 in Berlin; Vogel et al., 2019 in Paris; Makarova et
70   al., 2021 in St Petersbourg; Zhou et al., 2022 in Beijing and Xianghe; Che et al. 2022, in Beijing; Rißmann et al.,
71   2022 for Munich) coupling columnar measurements with inverse modelling. Most of these studies were based on
72   short-term campaign observations, applying the Differential Column Methodology (DCM, Chen et al., 2016) or
73   dedicated dispersion models (Hase et al., 2016), coupled with simple mass balance-based methods or inverse
74   modelling to derive emissions. Most of these studies reported significant discrepancies between the estimates,
75   depending on the models used (Viatte et al., 2017).

76   In this study, we aimed to determine the Mexico City Metropolitan Area (MCMA) CO_2 and CO
77   emissions using ground-based FTIR and surface measurements, without resorting to complex dispersion and/or
78   chemistry transport models. The MCMA, with a population around 22 million inhabitants, is in the top ten most
79   populous cities in the world and ranks among the major emitters of GHGs in North America. The available
80   information of GHGs emission estimates are mainly based on the inventories reported by the Ministry of the
81   Environment of Mexico City (SEDEMA), which is updated every two years, but lagging several years behind. In
82   the report based on 2018, the latest published before the COVID19-lock-down (2020), a total emission of 75.2
83   Mt CO2-eq is estimated for the MCMA, 87% of which is attributed to fossil fuel combustion and 58% originates

from the transport sector (SEDEMA Inventory, 2018). The Mexico City government is actively engaged in the C40 Climate Change Program and implemented significant policy measures since 2008, including promoting sustainable transportation systems, implementing energy efficiency measures, increasing the use of renewable energy sources, and adopting green building practices. On a national scale, the country is committed to reduce its GHGs emissions by 35% by 2030 with respect to its base level, as stated in the last Nationally Determined Contributions report (NDC-2022, UNFCCC). To assess the effect of the national and local mitigation policies, the installation of ground-based GHG measurement networks and the refinement of bottom-up estimates by comparing them with the top-down method (i.e: inverse modelling) is of critical importance to obtain a comprehensive GHGs database that can serve as follow-up of the mitigation actions.

The Institute of Atmospheric Sciences and Climate Change (ICAyCC, Spanish acronym) at UNAM (Universidad Nacional Autónoma de México) deployed in the last decade a wide range of surface gas sensors and ground-based remote sensing instruments across the MCMA (Grutter, et al., 2003; Molina et al., 2010; Bezanilla et al., 2014; Stremme et al., 2009; 2013; Baylon et al., 2017) in the frame of research projects related to air quality assessment, atmospheric monitoring and satellite products validation. Since 2013, UNAM has contributed to the Network for the Detection of Atmospheric Composition Change (NDACC), performing continuous composition measurements of the free troposphere from the high altitude Altzomoni Atmospheric Observatory (ALTZ) station, located 60 km southeast of Mexico City at 3985 m a.s.l. Baylon et al., (2017) reported the background CO_2 variability and trend from this station between 2013 and 2016. Stremme et al., (2013) reported the first top-down estimate of carbon monoxide (CO) emissions for the MCMA, based on FTIR CO total column measurements and the Infrared Atmospheric Sounding Interferometer (IASI) data. These authors derived the CO_2 emissions for the MCMA using the CO emission estimates and the average CO/CO_2 ratio reported in Grutter (2003), using FTIR measurements. In 2018, the Mexican/French "Mexico City's Regional Carbon Impacts (MERCI-CO2)" project (coordinated by UNAM and LSCE) was launched aiming to assess the CO_2 emissions from MCMA using EM27/SUN measurements and inverse modelling to evaluate the effectiveness of the mitigation strategies implemented by the local authorities. Xu et al., (submitted) examined the performance of a modelling system based on WRF-Chem to assess the whole-city emissions using the EM27/SUN measurements deployed in the frame of the MERCI-CO2 project. The complex orography of the region posed a challenge in the atmospheric transport simulations and thus for the top-down estimates using inverse modelling. Indeed, Mexico City is situated in a high altitude basin (~2300 m. a.s.l.), surrounded by mountains reaching up to 5.6 km a.s.l., and is prone to accumulate anthropogenic emissions, especially during the dry season, when the atmospheric boundary layer ventilation is limited (Burgos-Cuevas et al., 2023). The boundary layer dynamics in the basin and the wind surface circulation is complex, due to the temperature contrasts and rough topography.

In this study, we report the long-term (2013-2021) variability of the CO_2 and CO total columns and surface concentrations (from 2014) over the MCMA using ground-based FTIR and surface Cavity Ring-Down Spectroscopic (CRDS) measurements. Using the mixed layer height data from the continuous ceilometer measurements at UNAM, we examined the consistency of the surface and total column measurements of our network. We also determined an average CO/CO_2 ratio based on FTIR and surface measurements at different temporal resolutions (from daily to intraday). Then, using the spatial distribution of TROPOMI CO column

123   measurements, we explore the potential of our FTIR network to capture the variability of the megacity CO and

124   CO_2 emissions using a simplified model, i.e.: without recourse to complex numerical simulations. Our estimates

125   are compared with the available bottom-up and previous top-down estimates.

126   **2 Sites, instrumentation and measurement protocols**

127   We used in this study the column-averaged dry-air mole fractions of CO_2 and CO (XCO_2 and XCO)

128   from three permanent FTIR stations distributed in a radius of 100 km around MCMA (Fig. 1), and the surface

129   measurements performed at UNA and ALTZ sites. The measurement periods for the different instruments at

130   each site are reported in Table 1. The VAL station is located at the northern part of the city in a highly

131   industrialised zone. The UNA station is situated at the south of the city in the main campus of UNAM. The third

132   station is the ALTZ background site (3985 m a.s.l.), located 60 km ESE from UNAM, within the Izta-Popo

133   National Park. The equipment of the different stations and measurement protocols are described in the following

134   sub-sections.
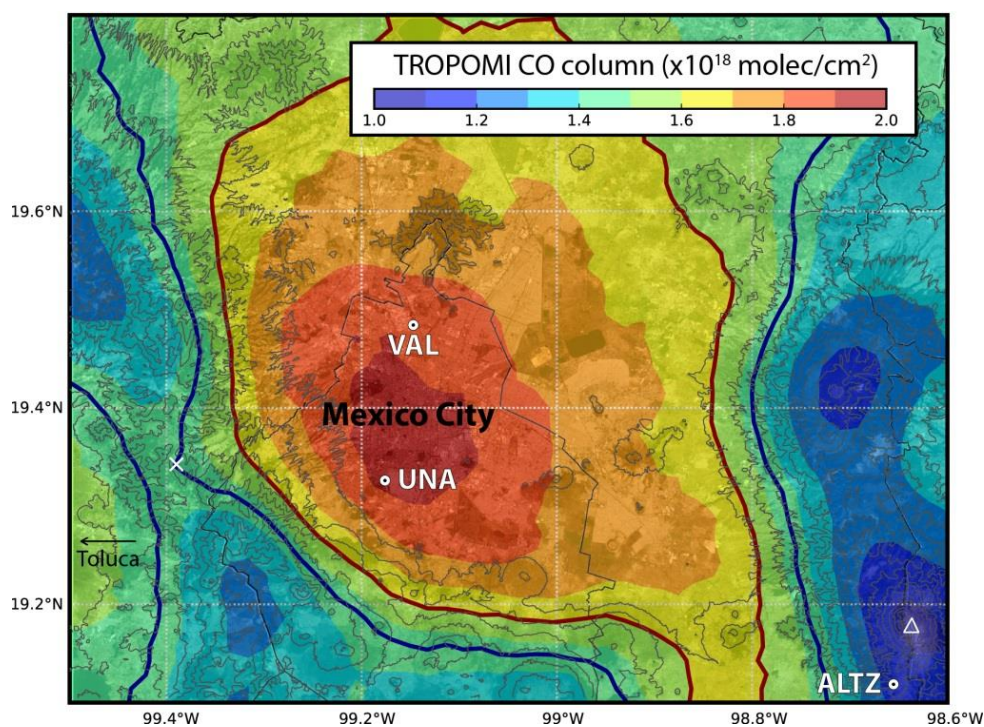
135

136   **Figure 1: Map of the ALTZ, UNA and VAL stations and average distribution (2018-2022) of carbon monoxide total**
137   **columns over the Mexico City Metropolitan Area (MCMA) calculated from the TROPOMI CO product. Red and**
138   **blue contour lines represent the inner and outer area used to calculate the effective area (see details in text). The cross**
139   **symbol indicates the smallest CO total column value observed upwind the city at the elevation of the Mexican basin,**
140   **which is used to estimate the background. The average total column can be decomposed into two main contributors: i)**
141   **a background of around 1.45×10^{18} molec.cm^{-2} (limits represented by blue contour lines) and ii) the local influence**
142   **corresponding to the carbon monoxide emitted on the same day. The total columns are highly influenced by the**
143   **topography which is clearly visible over the highest terrains of the region, near to the Popocatepétl and Iztaccíhuatl**
144   **volcanoes at the south east of Mexico City. The mountains of Ajusco are located southwest of Mexico City. The**
145   **enhancement in the center of the metropolitan area reflects the carbon monoxide locally emitted on the same day.**

146

147

148

149

Table1: Instrumentation and measurement periods used in this study.

Station	Instrument	Measurement period	Product
ALTZ (19.119°N, 98.655°W 3.99 km a.s.l.)	IFS120/5HR	01/01/2013 - 01/06/2021	XCO and XCO_2
	EM27/SUN #038	21/10/2020 - 20/12/2020 & 10/02/2021 - 22/02/2021	XCO and XCO_2
	EM27/SUN #104	07/02/2020 - 18/02/2020	XCO and XCO_2
	CRDS G2401 Picarro	15/11/2015 - 01/06/2021	Surface CO and CO_2
UNA (19.326°N, 99.176°W 2.28 km a.s.l.)	Vertex	15/11/2015 - 20/06/2017	XCO
	EM27/SUN #038	07/05/2021 - 25/05/2021	XCO and XCO_2
	EM27/SUN #062	17/03/2016 - 01/06/2017	XCO_2
		01/06/2017 - 01/06/2021	XCO and XCO_2
	EM27/SUN #104	04/04/2019 - 19/09/2019	XCO and XCO_2
	CDRS G2401 Picarro	15/11/2015 - 01/06/2021	Surface CO and CO_2
	CL31 Vaisala ceilometer	15/11/2015 - 01/06/2021	Mixed Layer Height
VAL (19.484°N, 99.147°W 2.26 km a.s.l.)	EM27/SUN #104	23/09/2019 - 01/06/2021	XCO and XCO_2

2.1 The UNA station: Total columns, surface concentrations and mixed-layer height measurements

Atmospheric total columns of several gas species, such as O_3, NH_3, CH_4, CO, and HCHO have continuously been measured at UNA since 2010 (Bezanilla et al., 2014; Plaza-medina et al., 2017; Baylon et al., 2017; Rivera-Cardenas et al., 2021; Herrera et al., 2022) using solar absorption FTIR spectroscopy.

Measurements are performed in the mid-infrared (MIR) and near-infrared (NIR) spectral ranges using a Bruker model Vertex 80 spectrometer. The instrument has a Maximum optical Path Difference (MPD) of 12 cm (corresponding to a spectral resolution of 0.075 cm^{-1}) and is equipped with two detectors, a liquid-nitrogen cooled mercury-cadmium-telluride (MCT) and InGaAs detectors. Solar absorption measurements are performed using a home-built solar tracker. A full description of the instrumental set-up and measurement protocols is given in Bezanilla et al. (2014) and Plaza-Medina et al. (2017). The CO measurements are routinely performed in the MIR spectral range with a spectral resolution of 0.1 cm^{-1}, using the MCT detector.

In March 2016, an EM27/SUN spectrometer was implemented at UNA to continuously measure XCO_2, XCH_4, XH_2O, XCO total columns from solar NIR spectra with a spectral-resolution of 0.5 cm^{-1} (MPD of 1.8 cm). The spectrometer is equipped with its own solar tracker (Bruker CAMTracker; Gisi et al., 2011) capturing and redirecting the solar beam into a RockSolid^{TM} pendulum interferometer equipped with a Quartz beamsplitter. The EM27/SUN, with serial number #62 installed at the UNA station (hereafter EM27-SUN_62), was initially operated with a standard InGaAs-diode detector sensitive to the 5500-11000 cm^{-1} spectral range, to which a second InGaAs detector with Ge filter was added in 2017 for CO measurements through a second channel (4000 – 5500 cm^{-1}) (Hase et al., 2016). Further details on the technical characteristics and systematic performance evaluation of the EM27/SUN spectrometer are given in Frey et al., (2019) and Alberti et al., (2022). The spectrometer was installed in a home-made protective box, including a remotely-controlled dome cover, a GPS and a PCE-THB-40 data-logger for precise timing and surface pressure measurements. Double sided forward-

173   backward interferograms are routinely recorded with a scanner velocity of 10 kHz, so that the recording time of

174   one measurement (averaging 10 IFGs scans) is close to one minute.

175   Additionally, CO_2, CO, CH_4 and H_2O surface measurements are continuously performed at the UNA

176   station using a Cavity Ring-Down Spectrometer (CRDS, model G2401 from Picarro Inc.). The CRDS

177   spectrometer uses a laser to quantify the spectral features of gas-phase molecules in an optical cavity offering

178   effectively of up to 20 km absorption path length. Frequency shifts are prevented with a high-precision-

179   wavelength monitor and temperature and pressure are precisely controlled by the analyzer. The quantification is

180   improved by the simultaneous spectral analysis of the measured gases. A calibration system using 3 gas

181   standards provided by the National Oceanic and Atmospheric Administration Earth System Research Laboratory

182   (NOAA ESRL), traceable to the WMO2007 scale, was set up in 2018 at UNA and in 2019 at ALTZ. Data

183   collected before the installation of the calibration systems were corrected with calibration coefficients obtained

184   in 2018. The sampling inlet using Synflex tubing was placed at 24 m a.g.l. at UNA station and includes a Nafion

185   air dryer, as described in detail by González del Castillo et al. (2022). Data are continuously collected at 0.3 Hz

186   rate and their uncertainties, calculated as the standard deviation of raw data over 1-minute intervals when

187   measuring calibration gases, are equal to 0.03 ppm at UNA (González del Castillo et al., 2022).

188   Finally, continuous mixed-layer height (MLH) measurements are performed since 2008 at UNA using a

189   CL31 ceilometer instrument (Vaisala). This is a robust commercial instrument which emits light pulses at 10

190   kHz repeating frequency at 910 nm using an indium-gallium-arsenide diode laser. It detects the backscatters

191   signal through a single lens with a silicon avalanche photodiode. The resulting backscattering profiles have a

192   vertical resolution of 10 m and reach an altitude of 7,500 m. The profiles have been used to retrieve MLH above

193   the city since 2011 (García-Franco et al., 2018).

2.2 The ALTZ background station: Total columns and surface measurements

194

195   The Altzomoni Atmospheric Observatory (ALTZ) was equipped with a high-resolution FTIR

196   spectrometer (model IFS120/5HR, Bruker) in 2012, capable of measuring atmospheric spectra in the NIR and

197   MIR spectral regions with 257 cm MPD, equivalent to a spectral resolution of 0.0035 cm^{-1}. The instrument is

198   installed into a container with a motorised dome cover on the roof and a microwave communication system (60

199   km line-of-sight to the university campus), which allows a fully-remote control of the instruments. When the

200   dome is open, a solar tracker (CAMTracker; Gisi et al., 2012) collects the solar beam and orients it toward the

201   spectrometer entrance. The spectrometer can be operated with KBr or CaF_2 beam splitters, 3 different detectors

202   (MCT, InSb, and InGaAs) and a set of 7 optical filters is installed in a rotating wheel. The measurement routine

203   consists in the acquisition of high (0.005 cm^{-1}), medium (0.02 cm^{-1} and 0.1 cm^{-1}) and low (0.5 cm^{-1}) resolution

204   spectra in the NIR and MIR spectral ranges using the different NDACC filters (~40 min for a complete

205   sequence).

206   The NIR CO and CO_2 spectra (0.02 cm^{-1}) used in this study were recorded as the average of two scans

207   taken for approximately 38 s with a scanner speed of 40 kHz. The MIR CO spectra (0.005 cm^{-1}) are deduced

208   from the coaddition of 6 scans (<200 s) with a scanner speed of 40 kHz. Due to a spectrometer laser

209   replacement, the IFS120/5HR measurements were interrupted between November 2020 and January 2021. To

210   avoid an important gap in the measurements, an EM27/SUN (EM27/SUN_38) was temporarily installed at the

211   station during this period (Table 1). The intercalibration factors used for combining the two types of

212 measurements were determined from previous side-by-side measurements performed during February 2021 (see
213 Table S1 and section 3.1.3).

214   A CRDS (model G2401 from Picarro Inc.) instrument was implemented at the station in 2014 providing
215 continuous CO_2, CO, CH_4 and H_2O surface measurements (Gonzáles del Castillo et al., 2022). The sampling
216 inlet using Synflex tubing was placed at 4 m a.g.l. and includes a Nafion air dryer (similar installation to UNA).
217 A calibration system similar to that implemented at UNA, using 3 NOAA ESRL gas standards, was set up in
218 2019. The station also includes meteorological instruments, pressure and temperature sensors and visible
219 cameras among other instrumentation for atmospheric and environmental monitoring.

2.3 The VAL station: Total column measurements

221   The VAL station, located in Vallejo in the northern part of MCMA, is part of the city's air quality
222 network (RAMA) run by SEDEMA. An EM27/SUN spectrometer (EM27/SUN_104) was installed at this station
223 in 2019 together with a surface CO_2 sensor. The VAL spectrometer has been performing measurements with the
224 two detectors since November 2019. Additionally, the VAL site included a low-cost medium precision CO_2
225 sensor, as a part of a network implemented during the MERCI-CO2 campaign. It consists of a NDIR-type of
226 sensor (SenseAir, model HPP3) that can measure in the 0 to 1000 ppm range and after a calibration and target
227 gas follow-up procedure, can produce data with <1% accuracy (Porras et al., 2023).

3.1 FTIR data processing and analysis

229   In this study, we used the solar absorption measurements acquired by five different FTIR instruments
230 (i.e: three EM27/SUN, a Vertex 80 and a IFS120/5HR) to estimate the XCO_2, and XCO total columns at each
231 station. The retrieval strategies were adapted as a function of the spectral resolution and averaging kernel of each
232 species. Table 2 summarises the different products used in this study, and their retrieval parameters.

233 *Table 2: FTIR analysis: Description of the different FTIR products, retrieval strategies and parameters used in this study.*

Instrument (spectral resolution)	Gas	Microwindows (cm^{-1})	Interfering gases	Retrieval code	Retrieval method
EM27/SUN and IFS-120/5HR LowRes (0.5 cm^{-1})	CO_2	6173.0 - 6390.0	H_2O, CH_4	PROFFAST	Scaling VMR COCCON strategy
	CO	4208.7 - 4318.8	H_2O, HDO, CH_4, HF		
	O_2	7765.0 - 8005.0	H_2O, CO_2, HF		
IFS-120/5HR (0.02 cm^{-1}) (TCCON-type)	CO_2	6180.0 - 6260.0 6310.0 - 6380.0	H_2O, CH_4, HDO	PROFFIT9.6	Scaling VMR
	CO	4208.7 - 4257.3 4262.0 - 4318.8	CH_4, H_2O, HDO		
	O_2	7765.0 - 8005.0	H_2O, CO_2 , HF		
IFS-120/5HR (0.005 cm^{-1}) (NDACC-type)	CO	2057.70 - 2058.00 2069.56 - 2069.76 2157.50 - 2159.15	O_3, N_2O, H_2O, OCS and CO_2	PROFFIT9.6	Profile NDACC strategy
Vertex80 (0.1 cm^{-1})	CO	2056.70 - 2059.00 2068.56 - 2069.77 2156.50 - 2160.15	O_3, N_2O, H_2O, OCS and CO_2	PROFFIT9.6	Profile

3.1.1 EM27/SUN spectra analysis

Double-sided interferograms from the EM27/SUN were analysed following the standardised COCCON protocol, using PREPROCESS and PROFFAST codes, developed by the KIT and made freely available (https://www.imk-asf.kit.edu/english/COCCON.php). The codes and retrieval methods are fully described in Sha et al. (2020), Frey et al. (2021) and Alberti (2023) and only briefly summarised here. The PREPROCESS algorithm generates the required spectra by a Fast Fourier Transform. The processing incorporates various quality checks, as a signal threshold, intensity variations during recording, requirement of proper spectral abscissa scaling, and generates spectra only from raw measurements passing all checks (the remaining ones being flagged). We used the ILS parameters (i.e: modulation efficiency amplitude and phase error) reported on the KIT-COCCON website (https://www.imk-asf.kit.edu/english/COCCON.php) and in Alberti et al. (2022), corresponding to the initial KIT calibration of the spectrometers (Frey et al., 2019, Alberti et al., 2022). The PROFFAST-PCXS module (i.e: forward model of PROFFAST) pre-calculates daily lookup tables of the molecular absorption cross-sections according to the meteorological parameters and gas trace VMR profiles priors. The latest PROFFAST-PCXS version uses the HITRAN 2020 spectroscopic linelists (with some extensions, e.g., line mixing parameters added for CH_4). Here, we used the standard COCCON linelists as incorporated in the previous PROFFAST version, i.e: HITRAN 2008 for CH_4, HITRAN 2012 for CO_2, a modified version of HITRAN 2009 by Toon (2014) for H_2O, a TCCON standard linelist for O_2, and the same solar line list as previously used by TCCON (compiled by G.C. Toon for GGG2014). The least-squares fitting code PROFFAST-INVERS retrieves the total columns by scaling the prior VMR profiles iteratively until adjusting the fit to the measured spectra. The intraday variability of surface pressure is considered in the retrieval, interpolated from the in-situ pressure measurements. For tying the column-averaged abundances provided by COCCON to TCCON data, PROFFAST applies post-process Airmass-Dependent (ADCF) and Independent (AICF) corrections, independent from the instrument, similar as used in the TCCON process (Sha et al., 2020, and Alberti, 2023). The corrections and parameters used are reported in the COCCON website and Alberti, (2023).

We automatized and adapted the data processing to obtain a preliminary "real-time" hourly-updated analysis (hereafter, AN1) for each site, additionally to the off-line treatment (hereafter, AN2) applying the standard COCCON procedure. The meteorological data used in the AN1 retrieval were derived from the daily-available radiosonde data, provided by Servicio Meteorologico Nacional (SMN) from measurements performed in the early morning (6 AM LT) at the Mexico City International Airport. The AN1 strategy adopted fixed VMR priors for each species, consisting in the averaged profile of 41 years (1980-2020) run of the Whole Atmospheric Community Climate Model (WACCM), as commonly used in the NDACC community. The AN2 processing, generating the COCCON standard products, used the daily TCCON meteorological data and priors (GGG2014 version of MAPs files), downloaded from the Caltech server, which are based on National Centers for Environmental Prediction (NCEP) reanalysis. For both AN1 and AN2 processing, we used the in situ intraday surface pressure measurements from the PCE-THB-40 sensors. A correction factor was applied to the pressure measurements to take into account the bias between the different pressure sensors used, previously intercompared by a few days of side-by-side measurements.

272    CO_2, O_2, and CO were analysed in the 6173.0 - 6390.0 cm^{-1}, 7765.0 - 8005.0 cm^{-1} and 4208.7 - 4318.8

273 cm^{-1} spectral windows, respectively. The XCO_2 and XCO column-averaged dry air mole fractions were

274 calculated using the O_2 retrieved total columns, according to Wunch et al. (2009):

275  $Xgas = 0.2095\,(C_{gas}\,/\,C_{O2})$                (1)

276 where C_{gas} and C_{O2} are the target gas and O_2 total columns, respectively.

277 The real-time (AN1) and COCCON (AN2) XCO_2 and XCO products showed relative differences lower than

278 0.05% and 5%, respectively. The results presented hereafter are based on the official COCCON products (AN2

279 analysis).

280 **3.1.2 Vertex80 and IFS120/5HR spectra analysis**

281    High (0.005 cm^{-1}) and medium (0.02 cm^{-1} and 0.1 cm^{-1}) resolution solar-absorption spectra are

282 processed using the PROFFIT9.6 code (Hase et al., 2004).

283 XCO_2 is retrieved from the NIR 0.02 cm^{-1} resolution spectra applying the procedure described in Baylon et al.

284 (2017), in which two independent CO_2 and O_2 VMR-scaling retrievals are performed using fixed WCCAM

285 VMR priors and NCEP-derived meteorological data. Spectral windows and interfering gases (Table 2) are

286 similar to those used in the standard TCCON procedure. XCO_2 is then calculated from the retrieved CO_2 and O_2

287 total columns by applying Eq. (1).

288 For the ALTZ analysis, CO was retrieved from the high (0.005 cm^{-1}) resolution spectra in the MIR region,

289 applying the standard NDACC procedure (Pougatchev et al., 1994; Rinsland et al. 1998; Table 2). It uses a

290 profile retrieval strategy with fixed WACCM VMR priors and NCEP meteorological data. Since the O_2 specie is

291 not analysed in the MIR region, the XCO was determined using the dry air columns (C_{dryair}):

292

293   $XCO = \dfrac{C_{CO}}{C_{dryair}}$               (2)

294   with:

295   $C_{dryair} = \left(\dfrac{P_g}{g}\,m_{dryair}\right) - \left(C_{H2O}\,\dfrac{m_{H2O}}{m_{dryair}}\right)$      (3)

296

297 where C_{CO} and C_{H2O} are the retrieved CO and H_2O total columns, g the column-averaged gravity acceleration, P_g

298 the ground pressure and m_{dryair} and m_{H2O}, the dry air and H_2O molecular masses respectively. In addition, we

299 analysed XCO from the NIR spectral region to complement the MIR time-series, occasionally interrupted when

300 the liquid nitrogen was missing at the station. The CO and O_2 columns in the NIR region were analysed using

301 scaling retrievals in the same spectral windows as that used by TCCON (Table 2), but with fixed WACCM VMR

302 priors and NCEP meteorological data. XCO was calculated from the CO and O_2 retrieved total columns applying

303 Eq. (1). To minimise the air mass dependence effect (likely low for CO), we filtered out data with a SZA >60°.

304 XCO NIR and MIR products were compared and intercalibrated (section 3.1.3).

305 For UNA, we used the XCO total columns calculated from the Vertex80 measurements to complement the

306 EM27/SUN time series during the period when it was operating with a single detector (between March 2016 and

307 September 2017). CO was analysed from the 0.1 cm^{-1} resolution spectra in the MIR spectral range, using a

308 standard NDACC profile retrieval strategy and the PROFFIT9.6 retrieval program with constant WACCM VMR

309 priors and NCEP meteorological data. Spectral windows (Table 2) were adapted following Pougatchev and

310 Rinsland (1995). Previous CO total columns time series retrieved from the same method at UNA were presented

311 in Garcia-Franco et al. (2018) and Borsdorff et al. (2018, 2020). Only the constraint of these CO retrievals were

312 adjusted for the Megacity and allowed in addition a free fitting of the mixing layer concentration, following the

313 work by Stremme et al. (2009) in which low resolution MIR spectra with a different retrieval program have been

314 analysed.

315 **3.1.3 Measurement precision and FTIR product intercomparison**

316 Side-by-side measurements were performed at the ALTZ and UNA stations on several occasions

317 (Table1) to assess the FTIR measurement precisions, to characterise the bias between the different products and

318 to define the inter-calibration factors for the XCO_2 and XCO products. We used the EM27/SUN_62 products as

319 reference, for which we previously applied the standard XCO_2 and XCO calibration factors reported in Alberti et

320 al. (2022), to inter-calibrate our results with the COCCON network and the Karlsruhe TCCON station operated

321 by KIT. The linear regression parameters from the different measurement pairs and the calibration factors are

322 presented in the Supplementary data (Table S1 and S2).

323 We found a bias lower than 0.2% and 1.0% between the three EM27/SUN, for XCO_2 and XCO respectively, and

324 a coefficient of determination (R^2) higher than 0.99.

325 On the other hand, the precision of the EM27/SUN measurements was assessed by calculating the standard

326 deviation over a 5 min-interval period, and found to be on average 2.7 ppb and 0.3 ppm for XCO and XCO_2,

327 respectively.

328 The intercomparison of the IFS120/5-HR high resolution (0.02 cm^{-1}) products and the EM27/SUN XCO_2

329 products was performed for the daily average data used in this study. The calibration factors were determined

330 using i) the EM27/SUN XCO_2 products and ii) the IFS 120/5-HR low resolution (0.5 cm^{-1}) product (Fig. S2),

331 processed in the same way as the COCCON EM27/SUN data but having the advantage of being measured even

332 outside the campaigns carried out with the EM27/Sun. We finally found a bias around 0.4% (slope=0.996), and a

333 coefficient of determination R^2 of 0.92. This bias is of order of that expected when comparing TCCON and

334 COCCON products (Frey et al., 2019), when no empirical calibration is applied. On the other hand, a bias of 2%

335 (and R^2=0.92) was found comparing the XCO from the EM27/SUN and the Vertex (MIR) products at UNA.

336 One of the main contributions of the apparent bias observed when comparing products from different

337 instruments and using different retrieval strategies can be due to their respective Averaging Kernel (AK) which

338 characterise the smoothing error. It is especially the case in the comparison of XCO from the EM27/SUN (i.e:

339 NIR scaling retrieval product, Degree Of Freedom (DOF) =1) and from the Vertex (MIR profile-product, DOF >

340 2). To assess this effect, we refined the comparison after smoothing the vertically resolved Vertex profiles with

341 the EM27/SUN AK (following Rodgers, 2000; Borsdorff et al., 2014, 2018) and re-calculating the smoothed

342 Vertex total columns. After this smoothing, the bias is reduced to 0.2% instead of 4.1% for the CO total

343 columns. For the XCO product, which includes the use of the surface pressure for the MIR product and the

344 retrieved O_2 column for the NIR product the bias is reduced to 0.4% instead of 3.5%.

3.2 Surface CRDS data analysis

The surface CO_2 and CO data acquired with the CRDS analysers were processed and averaged following the procedure described in González del Castillo et al. (2022). Data were averaged and their standard deviation calculated, per minute, then per hour. To extract the trend and seasonal CO and CO_2 variability, data were filtered by discarding hours generally affected by transient and very local effects. Data recorded between 13 and 17h with standard deviations lower than 6.0 ppm were selected for the UNA station, while nighttime data (19 to 5h) with standard deviations lower than 2.0 ppm were selected for the ALTZ station, according to González del Castillo et al. (2022).

3.3 Mixed Layer height from the Lidar measurements

The MLH is retrieved using a combined algorithm based on the gradient method and a wavelet-covariance transformation as described in detail by García-Franco et al. (2018). These results were compared with radiosonde data and MLH values derived from surface and vertical column densities of trace gases, and more recently Burgos-Cuevas et al. (2022) used the variance of the vertical velocity from a Doppler Lidar (Wind Cube 100, Leosphere) and compared with the ceilometer results at the same location. These studies show that the ceilometer retrieved MLHs compare well with other techniques during the daytime (they agree within 15% with the trace gas method), which are relevant for this study, whereas late afternoon and nighttime retrieved values might be affected by aerosol residual layers at higher altitudes.

3.4 Mixed layer CO and CO_2 concentrations from FTIR measurements

Pollutant concentrations within the mixed layer are often estimated using surface measurements, although surface concentrations are very sensitive to the airmass vertical transport, unlike the total columns. It is especially the case within the Mexico City basin where the mixed layer has a strong diurnal dynamics controlling the vertical distribution of the emitted pollutants (Stremme et al., 2009; Garcia-Franco et al., 2018). An estimate of the CO_2 and CO vertically averaged concentrations across the mixed layer can be made using the total columns measured at the UNA and ALTZ stations. The dry air mole fraction measured at the UNA station (XCO_2^{UNA}) is the weighted mean of that measured in the mixed layer (CO_2^{ML}) and in the free troposphere at the ALTZ station (XCO_2^{ALTZ}):

$$XCO_2^{UNA} = w_1 \times CO_2^{ML} + w_2 \times XCO_2^{ALTZ} \tag{4}$$

$$CO_2^{ML} = \frac{XCO_2^{UNA} - w2 \times XCO_2^{ALTZ}}{W1} \tag{5}$$

(5)

The weights (w1 and w2) depend on the pressure difference between the mixed-layer height (MLH) and the UNA station, the pressure on top of the mixed layer is calculated assuming an exponential decay and an effective scale height H_{scale} (assumed to be 8.0 km):

$$w_1 = \left(1 - e^{-\frac{MLH}{Hscale}}\right) \text{ and } w_2 = \left(e^{-\frac{MLH}{Hscale}}\right) \tag{6}$$

378   The MLH above Mexico City was estimated using the hourly-averaged measurements of the ceilometer at the

379   UNA station. The hourly-averaged CO_2^{ML} and CO^{ML} products were calculated applying the same strategy for the

380   entire time series and are reported in Fig. 7, concurrently to the surface data.

381   **4 Results**

382   The FTIR XCO_2 and XCO daily-averaged time series and CO_2 and CO surface concentrations obtained at the

383   UNA, VAL and ALTZ stations between November 2015 and June 2021 are shown in Fig. 2. Trends and

384   seasonal variabilities were fitted using a Fourier series analysis (Eq. (7) and black and red solid lines in Fig. 2),

385   following Wunch et al. (2013):

386

387     $f(x) = ax + \sum_{k=0}^{n} a_k \cos(2\pi kx) + b_k \sin(2\pi kx)$, with $n = 2$ (7)

388

389   where x is the time (decimal year), a the mean growth rate (ppm/year), and a_k and b_k the Fourier coefficients

390   modulating the annual cycles. The coefficients for each gas species and station are reported in Table 3.

391
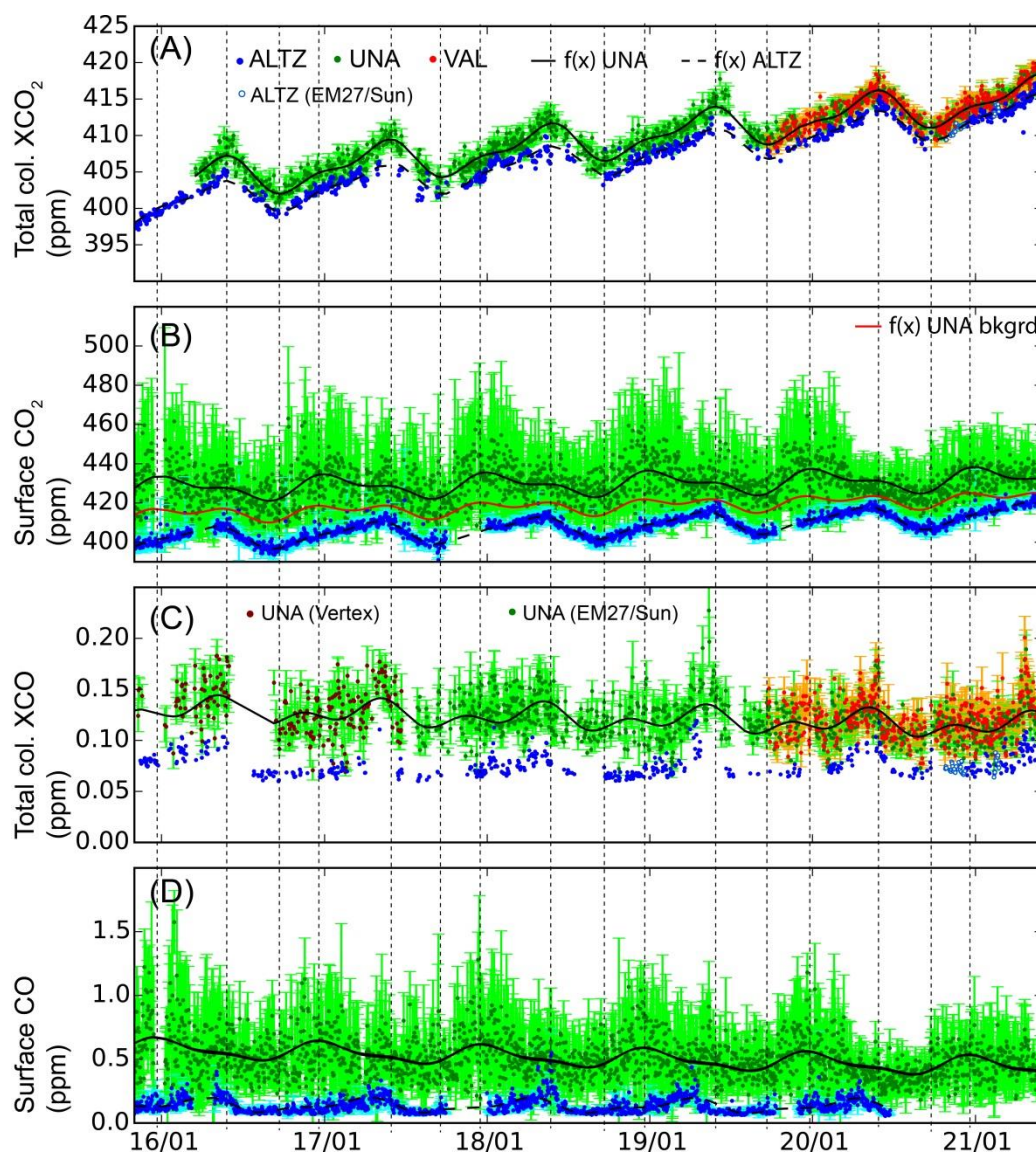
Figure 2: Time series of (A) the total column XCO_2 from the FTIR measurements (B) the CO_2 surface concentration from the CRDS measurements, (C) the total column XCO from the FTIR measurements (D) the CO surface concentration from the CRDS measurements for the UNA (in green), VAL (in red) and ALTZ (in blue) stations. For each time series, the daily average data are presented as dots with their daily standard deviations. Black traces show the annual fit calculated from the Fourier series (Eq. (7)). In (A) and (C), we distinguished between ALTZ data obtained from the IFS120/5HR (blue full circles) and from the EM27/Sun (blue open circles) and in (C), between the CO total columns obtained from the VERTEX instrument (in brown) and the EM27/Sun (in green) at the UNA station. In (B) the red curve corresponds to the background fit, calculated following Gonzalez del Castillo et al. (2022), to determine the annual trend and seasonal cycles. Vertical dash lines highlight the minimum and maximum of the annual cycles for the different products.

4.1 Trends and interannual variability

The total column XCO_2 time series (Fig. 2A) at ALTZ and UNA show a similar mean growth rate around 2.4 ppm/year (2.4 and 2.3 ppm/year for ALTZ and UNA, respectively, Table 3) over the whole measurement period. A similar mean growth rate is also found for the surface CO_2 time series (Table 3 and Fig. 2B) in ALTZ (2.5 ppm/year). These values are consistent with those estimated at the Mauna Loa Observatory (MLO) reference station for the 2016-2021 period (average of 2.5±0.5 calculated from surface data available in the NOAA site https://gml.noaa.gov/ccgg/trends).

Table 3: Fourier series fitting parameters for the UNA, VAL and ALTZ XCO_2 and XCO time series presented in Fig. 2, and calculated from Eq.(7).

Fitting parameters (ppm/year)	XCO_2, UNA Tot. Col.	XCO_2 ALTZ Tot. Col.	CO_2 UNA Surface	CO_2 ALTZ Surface	XCO UNA Tot. Col.	CO UNA Surface
a	2.25±0.02	2.40±0.01	1.6±0.1	2.48±0.02	$(-4.0\pm0.8)\times10^{-3}$	$(-2.7\pm0.1)\times10^{-2}$
$a1$	-1.06±0.04	-0.78±0.04	1.7±0.2	-0.39±0.05	$(-2.4\pm0.7)\times10^{-3}$	$(6.5\pm0.4)\times10^{-2}$
$a2$	2.11±0.04	1.93±0.04	1.1±0.2	-0.36±0.05	$(-3.2\pm0.8)\times10^{-3}$	$(1.5\pm0.4)\times10^{-2}$
b1	0.71±0.04	0.64±0.04	2.1±0.2	4.62±0.05	$(8.6\pm0.8)\times10^{-3}$	$(6.5\pm4.0)\times10^{-3}$
b2	-0.78±0.04	-0.45±0.04	-2.1±0.2	-1.69±0.05	$(-7.9\pm0.7)\times10^{-3}$	$(-2.2\pm0.4)\times10^{-2}$

At the UNA station a surface mean growth rate of 1.6 ppm/year is found, lower than that observed from the total column measurements. Comparing the surface mean growth rates with those reported by González del Castillo et al. (2022) for the 2014-2019 period, we observe a significant difference for the UNA station (2.3 ppm/year in González del Castillo et al., 2022) but very similar values for the ALTZ station (2.6 ppm/year in González del Castillo et al., 2022). The difference observed at UNA could stem from (i) starting our new time series at the end of 2015, when the annual growth rate is maximum (González del Castillo et al., 2022) and (ii) the inclusion of the 2019-2021 period, when the mean growth rate clearly decreased. At the VAL station, the total column XCO_2 time series are found very similar to those observed at UNA stations (Fig. 2A). Figure S1 shows that 86% of the daily average data at VAL and UNA have a difference lower than 1.0 ppm, although a large part of the

423 comparison was done during the COVID19 lock-down period (Table1), for which lower gradients are expected

424 due to the decrease of the anthropogenic emissions.

425 The interannual variability can be explored through the time series of the mean annual growth rate (AGR) and

426 the monthly-sampled annual growth rate (MAGR), according to Buchwitz et al. (2018). The MAGR is calculated

427 by month, as the difference between the monthly-average Xgas data of a year i and the monthly-averaged data of

428 the previous year ($i-1$). The AGR is obtained for each year, averaging all of the MAGR. The AGR and MAGR

429 for total column and surface measurements are presented in Fig. 3. We include data from the MLO in Fig. 3A,

430 for which the AGR (dashed black curve) was derived from the surface data available in the NOAA site.

431
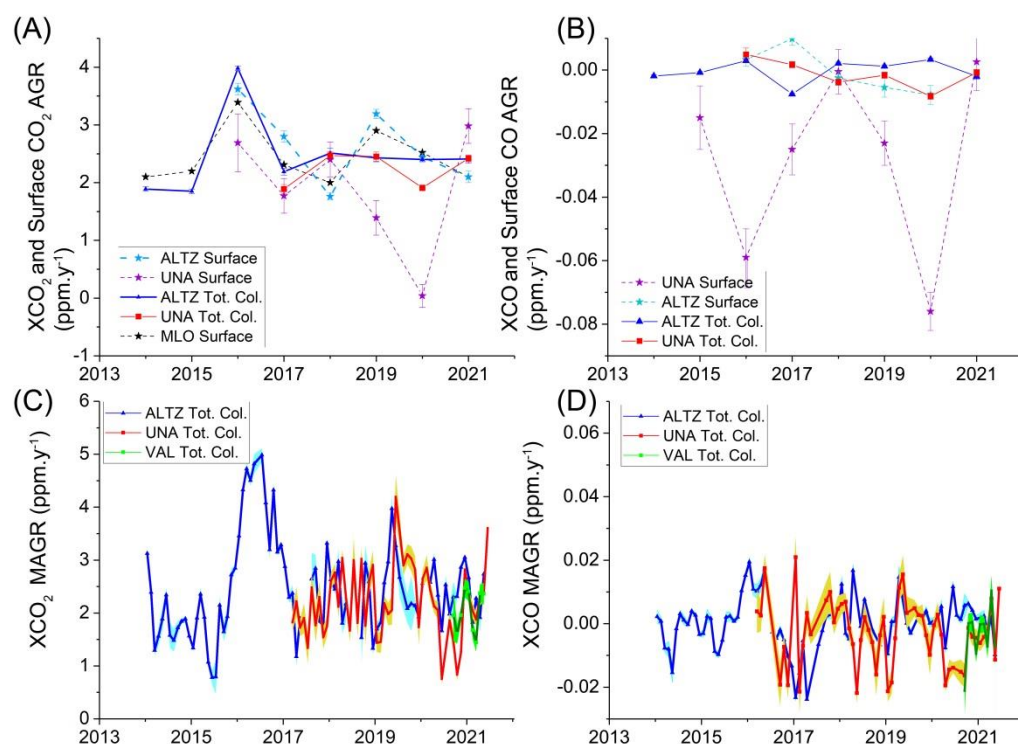
Figure 3: XCO_2 (A) and XCO (B) annual growth rates (AGR) and XCO_2 (C) and XCO (D) monthly-sampled annual growth rate (MAGR) obtained from total column and surface measurements for UNA, VAL, and ALTZ stations. In (A), the Mauna Loa (MLO) AGR trend was added in black dash-line. In (A) and (B) errors bars represent the standard error after removing annual cycles, reflecting the data sample quality. The standard error for the MAGR is shown as shaded area in (C) and (D).

437 At ALTZ, the interannual variability of the total column XCO_2 AGR (Fig. 3A) was found similar to that

438 obtained from both the ALTZ and MLO surface data, with a coincident peak in 2016, reaching an AGR value of

439 3.5 (surface data) and 4.0 (total column data) ppm/year. Surface data AGR time series show a second peak in

440 2019, which is not apparent for the total column XCO_2 time series. The time series of the MAGR (Fig. 3C)

441 allows better identifying and characterising the period and duration of the anomalies. The 2016 XCO_2 anomaly

442 has a duration up to 15 months (from October 2015 to March 2017), reaching a maximum value (around 5.0

443 ppm/year) between March and July 2016, corresponding to a factor of 2.8 higher than the 2013-2015 base level

444 (1.8 ppm/year).

445 At UNA, the XCO_2 AGR and MAGR time series (Fig. 3A and 3C) are very similar to those observed at the

446 ALTZ station, except for the year 2020. During this year, the AGR dropped by ~20% at UNA before returning in

447 2021 to the level of the previous two years. This behaviour contrasts with the AGR observed at ALTZ, which

448 remains nearly constant between 2017 and 2021. The MAGR time series at UNA (Fig. 3C) shows that this drop

449 is dominated by the exceptionally low June and October growth rates, representing the lowest MAGR values of
450 the UNA time series. This observation is supported by the VAL MAGR, although the time series is much
451 shorter. The surface CO_2 AGR at UNA shows a much higher interannual variability, with the strongest anomaly
452 observed in 2020, where the AGR is close to zero. A very clear decrease of the day-to-day and intraday CO_2
453 surface variability is observed in Fig. 2B from April to mid-September 2020, consistent with the XCO_2 MAGR
454 anomaly.

455 Upon examining CO, the UNA XCO time series (Fig. 2C) has daily averages ranging between 0.10 and
456 0.23 ppm with a mean and standard deviation of 0.12 and 0.02 ppm, respectively, but shows a decreasing rate (-
457 4.0×10^{-3} ppm/year) over the whole measurement period. The VAL XCO time series show a very similar baseline
458 to UNA, with a daily average difference lower than 0.02 ppm for 85% of the coincident dataset (Fig. S1). At the
459 ALTZ background site, the XCO baseline and day-to-day variability are lower than at UNA and VAL, as
460 expected (mean and standard deviation equal to 0.08 and 0.01 ppm, respectively). The surface CO time series
461 (Fig. 2D) shows a more significant decreasing trend (-2.68×10^{-2} ppm/ year) than the total column data at UNA,
462 while the baseline at ALTZ remains constant around 0.11 ppm. The CO AGR and MAGR at ALTZ and UNA
463 are shown in Fig. 3B and D. Generally, the XCO AGR and MAGR oscillate around their base level at the ALTZ
464 and UNA stations, with short-term anomalies. At ALTZ, a strong negative XCO AGR anomaly is observed in
465 2017, which was not observed for XCO_2, likely resulting from the exceptionally high XCO columns measured
466 during 2016. This is supported by the increase of the XCO MAGR from October 2015 to July 2016 (Fig. 3D),
467 coinciding with the first 10 months of the highest XCO_2 anomaly and followed by the lowest XCO MAGR
468 values of the time series (around -0.02 ppm/year in April 2017). At the UNA station, the AGR slightly decreases
469 between 2016 and 2020 and increases again in 2021. The most significant and prolonged (>5 months) MAGR
470 anomaly (Fig. 3D) occurred between April and September 2020, with negative values. Some short-term
471 additional anomalies are observed, but only a few of them (in May 2018 and January 2019) are not affected by
472 the limited number of available measurements.

473 **4.2 Seasonal variability and short-term cyclic events**

474 Annual cycles are observed for both total column XCO_2 and CO_2 surface measurements at ALTZ, UNA
475 and VAL stations (Fig. 2). The maximum and minimum of the total column XCO_2 cycles are observed in May-
476 June and September, respectively, with an average amplitude around 5 (ALTZ) and 6 (UNA) ppm.
477 To examine the temporal changes in amplitude and shape of the annual cycles, total column data were monthly-
478 averaged, detrended by subtracting the linear part of the fit ($f(x) = ax$, in Eq. (7)), and compared to the detrended
479 mean annual cycle ($f(x) - ax$) in Fig. 4. To obtain a longer-term view, we included the 2013-2015 period from the
480 ALTZ station, previously published in Baylon et al. (2017), after applying the inter-calibration factors (section
481 3.1.3). At ALTZ, two periods significantly deviated from the average XCO_2 seasonal cycle, i.e.: (i) the year
482 2015, where all the monthly averaged XCO_2 are below the fit and with one of the lowest seasonal amplitudes
483 (~4.0 ppm, Fig. 4A and 4C) of the whole time series, and (ii) the year 2016, with higher monthly averages than
484 the mean XCO_2 seasonal cycle and the highest amplitude (~5.8 ppm, Fig. 4A and 4C). At UNA, the difference
485 with respect to the average XCO_2 seasonal cycle is not significant, except for the year 2020, where all the
486 monthly averages are below the mean annual cycle (Fig. 4C). During this period, the UNA and VAL XCO_2
487 monthly-averaged data fit exceptionally well with those of the ALTZ station between March 2020 and March

488   2021 in terms of shape and amplitude, while the UNA and VAL annual cycle amplitudes are slightly higher than

489   those of ALTZ for the other years.
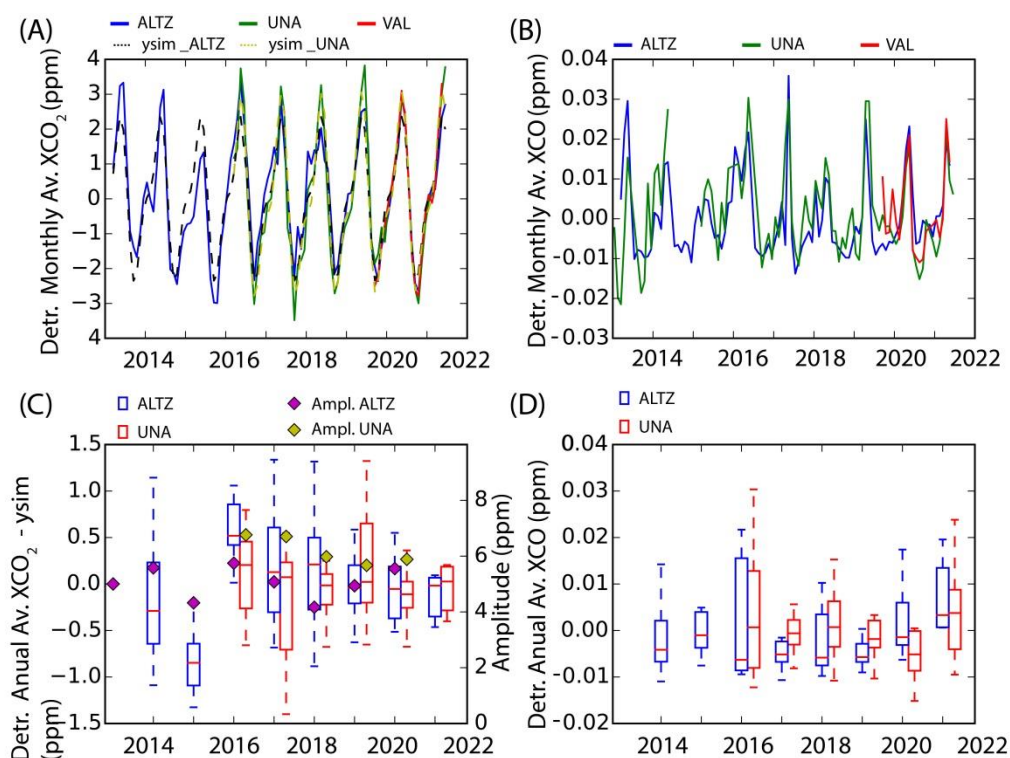
491   **Figure 4: Interannual and annual variability of the detrended XCO$_2$ and XCO total column data at the UNA, VAL**
492   **and ALTZ stations. In (C) and (D) the whisker diagrams are calculated from the monthly average detrended data.**
493   **The amplitude is determined as the max-min values.**

494   Regarding the CO$_2$ surface data (Fig. 2B), annual cycles are observed with maxima and minima reached mid-

495   December and mid-September, respectively. As also reported in González del Castillo et al. (2022), the

496   maximum occurred during winter, when shallower boundary layer prevails and the summer-autumn minimum

497   can be explained by the dilution of trace gases in a deeper convective boundary layer and more active urban

498   vegetation.

499   XCO peaks every year in April-May at the three stations (Fig. 2C and Fig. 4B) and then shows minimal annual

500   values in August, preceding by 1 month the minimum and maximum values of the XCO$_2$ time series. The April-

501   May maximal annual values, also confirmed by TROPOMI measurements (Borsdorff et al., 2020), coincide with

502   the biomass burning season and the periods during which the mixed layer reaches its maximum altitude (García-

503   Franco et al., 2018). During 2015, the XCO time series show a very low maximum reached in February instead

504   of May (Fig. 4B), contrasting with 2016, where high total column XCO values are reached in January and

505   maintained for a period of at least 5 months. 2016 also corresponds to the year with the highest XCO variability

506   of the time series (Fig. 4D). Additionally, in 2018, the XCO annual cycles differ from the other years with lower

507   values and a flat shape during the first semester of the year (January-May).

508   Surface CO data (Fig. 2D) also show periodic increases at the ALTZ station with maxima reached during April-

509   May, coinciding with the maxima observed from total column XCO measurements. They confirm the increase of

510   the CO emissions during the biomass burning season, at least dominant in the ALTZ measurements. However, at

511   the UNA station, cycles are also observed in the surface data but with a maximum coinciding with that of the

512   CO_2 surface data, and lagging behind the XCO total columns. These cycles are likely dominated by other

513   processes affecting both CO and CO_2 species such as the mixed layer seasonal dynamic.

4.3 Intraday variability

515   The intraday variability of the total columns and surface data are depicted in Fig. 5 and Fig. 6. Since the

516   ALTZ total column data do not present a significant diurnal pattern (the hourly variability remains lower than the

517   standard error of the time series), they are not presented in these plots.

518
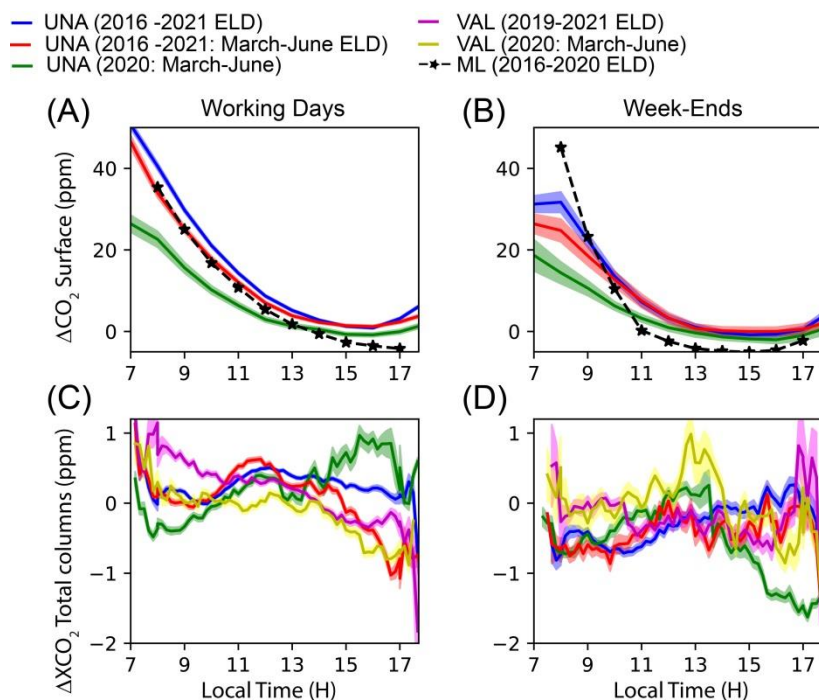
Figure 5: Diurnal patterns of the detrended surface CO_2 mole fractions (A and B) and XCO_2 total columns (C and D) measured at UNA and VAL stations. For each panel, the different curves represent different time periods: in blue, the whole measurement period excluding the lock-down (March-June 2020) period, in green the lock-down period (March-June 2020) and in red the whole measurement periods only including the March to June months and excluding the lock-down period. The standard errors are presented as shaded areas. Black curves represent the diurnal pattern of CO_2 in the Mixed Layer (ML) calculated from the total columns data for the UNA station.

525

526
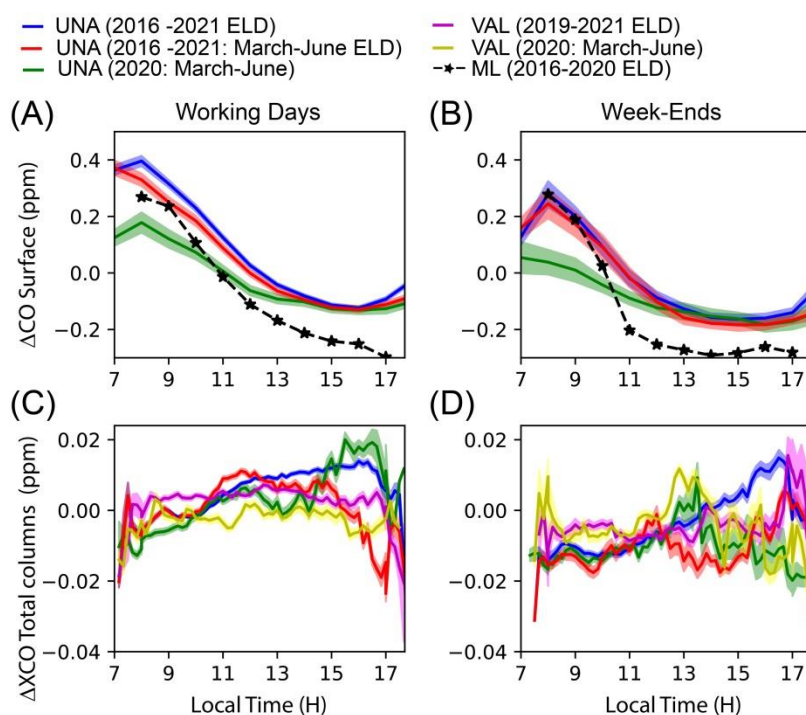
Figure 6: Same as Figure 5, but from surface CO and total column XCO measurements.

Total column data were detrended by removing the seasonal fit (black traces in Fig. 2A and Fig. 2C), and averaged over 10 min. To avoid a possible bias due to strong ventilation periods, a filter based on a ventilation index (VI) was applied, following recommendations in Hardy (2001), Su et al. (2018) and Storey and Price (2022). The VI is calculated as the product of average wind speed velocity (between the surface and 100 m height), and the planetary boundary layer height for UNA and VAL locations. The wind velocity and the MLH were estimated with the U and V wind components and the PBL height fields from the hourly ERA5 reanalysis product (Hersbach et al., 2020). In the MCMA, the surface wind speed presents a diurnal pattern, generally reaching a maximum during the afternoon between 14 and 15h LT (Fig. S4). The filter selects the days complying with the following criteria (i) a maximum wind velocity (average 10-100m height) between 10h and 12h LT lower than 1.5 m.s^{-1} (threshold based on Stremme et al., 2013) and (ii) a daily VI lower than 2350 m^2.s^{-1}, which represents a commonly used threshold for selecting poor ventilation conditions (Hardy, 2001; Storey and Price, 2022). About 60% of the original XCO$_2$ and XCO dataset is selected by applying the filter, and will be considered in the following analysis. We note that about 70% of discarded data corresponds to the January-May period of the year. Filtered total column XCO$_2$ and XCO data were averaged by 10 min and presented in Fig. 5C and 5D and Fig. 6C and 6D, distinguishing between the working days (WD) and the week-end (WE) periods. To explore the 2020 lock-down influence on the diurnal pattern, three different periods were distinguished for each plot, the first one (blue trace: 2016 - 2021) corresponding to the whole measurement period excluding the interval between March and June 2020 corresponding to the lock-down period (hereafter, called "ELD" for "excluding the lock down period"), where a significant MAGR decrease was observed; the second (green trace: March- June 2020) only includes the lock-down period, and additionally excludes the rainy season to avoid bias due to incomplete daily time series; and the third period (red trace) is the same as the first one, but only considering the March to June months to be compared with the lock-down period.

Surface data from the CRDS analyzers were detrended by removing the background fit following the methodology described in the section 3.2, and filtered to be coincident with the filtered total column measurements (selection of data between 7 and 18 h LT and only including the days with low ventilation conditions). They were finally averaged by hours and presented in Fig. 5A and 5B and Fig. 6A and 6B for the WD and WE periods, respectively, for which each curve represents the periods mentioned above.

The surface CO_2 diurnal pattern at UNA station for the whole measurement period (2016-2021, Fig. 5A and 5B in blue) is consistent with the one previously described in Gonzalez del Castillo et al. (2022) for the 2014-2019 period, with a maximum observed during the early morning (reached before 7h LT), a minimum during the afternoon (between 15 and 16h LT) and an average amplitude around 45 ppm. A lower amplitude of these cycles is observed at WE (average amplitude of 28 ppm) with respect to the WD periods. During the 2020 lock-down period (green curve), the WD surface CO_2 diurnal profile has a comparable amplitude (average amplitude of 26 ppm) to those of the WE for the whole measurement period, and slightly higher than that observed during the lock-down WE periods (average amplitude of 22 ppm). The surface CO diurnal profile (Fig. 6: 2016-2021, blue curve) peaks at 8h and then decreases until 16 h LT during any day of the week. The WD and WE data shows amplitudes of up to 0.5 ppm and 0.3 ppm, respectively. During the lock-down period the WD and WE amplitudes are much lower (0.3 and 0.2, respectively), consistently with the CO_2 surface observations.

The XCO_2 and XCO diurnal patterns (Fig. 5C and 5D and Fig. 6C and 6D) have very different shapes than those of the surface data, with amplitudes one order of magnitude lower. The variability observed between 7 and 8h is likely due to the low number of measurements during this time interval, and will not be taken into account in the following analysis. The UNA and VAL XCO_2 diurnal patterns significantly differ in shape. The VAL WD curve (magenta) continuously decreases from 8h to 17h (amplitude around 2 ppm) during both the whole measurement and lock-down periods, but during the lockdown period, lower values are generally recorded with higher intra-hour variability between 11h and 14h. The general WD decreasing trend suggests a maximum reached during the early morning (before 7h LT). This observation is supported by the CO_2 surface measurements performed with the low-cost medium precision CO_2 sensors (Porras et al., 2023), recording a maximum between 6h and 7h LT. The UNA XCO_2 WD diurnal pattern (blue trace) is almost constant until 10h, then increases until reaching a maximum around 12h, slightly decreases until 17h LT and finally shows an abrupt decrease after that. The amplitude of the diurnal variability is around 1 ppm. During the lock-down period, the diurnal profile is different, increasing until 12h LT, slightly decreasing until 13h LT and then increasing again until reaching a maximum at 16h, and finally abruptly decreasing until 17h LT. The lock-down WD XCO_2 profile shows lower values than the other periods until 13h, but the peak observed at 16h is not apparent for the other periods. Variability is generally lower at WE (<1ppm), except for the lock-down period, for which an important decrease is observed after 14h LT, but it is likely affected by a low number of measurement days. For XCO, the diurnal profiles also have different shapes at UNA and VAL. At UNA, the March-June XCO diurnal profiles (red and green curves) resemble that of XCO_2 for both the lock down and whole measurement periods. When considering the twelve months of the year (blue trace), the maximum curve slightly increases between 12h and 16h, when it reaches its maximum. It contrasts with the variability of the March to June months curves during this time interval, for which an increase is observed during the lock-down period or a decrease if considering the whole measurement period. At VAL, the diurnal profile is fairly constant until 17h with slightly lower values during the lock-down period.

591   The total column XCO diurnal profiles at WE are less reliable with larger standard errors, likely due to the low

592   number of considered measurements. An increase is nevertheless observed at UNA where the considered day's

593   number is statistically more reliable, with a peak around 17h LT, which was not observed for XCO_2.

594   The difference observed between the diurnal pattern of the XCO and XCO_2 at VAL and UNA is likely due to the

595   different advection drivers in the region mainly controlled by the topography. A Northern surface wind direction

596   (Fig. S6) is generally dominating over the Mexican valley but is locally highly influenced by the mountainous

597   barriers. The West-northwest wind component at UNA is likely to be the effect of down-slope flows from the

598   mountain ridge in the early morning (6 – 9 LT mostly), while at VAL, the plateau-to-basin winds are the main

599   influx into the basin coming from the northwest in the morning. There can also be an influence from an up-

600   valley flow in the mornings (de Foy et al., 2006). More generally the VAL station is likely influenced by the

601   north mountain, generating a significant gradient in the CO distribution upwind of the VAL station (Fig. 1). In

602   contrast, near the UNA station, the flat ground allows a more efficient mixing and due to the dominant North-

603   Northeast wind component in the late morning, the captured airmasses likely often reflects the MCMA plume

604   emissions.

605   **4.4 CO and CO_2 within the mixed layer from FTIR and surface data.**

606   Figure 7 shows the hourly-averaged CO_2 and CO concentration within the mixed layer (CO_2^{ML} and CO^{ML}

607   products), calculated from the FTIR measurements (see section 3.4), concurrently to the surface data. The CO_2^{ML}

608   and CO^{ML} products are in agreement with the surface observation, with a slope of 0.95±0.02 (R^2=0.74) for CO_2

609   (Fig. 7C) and 0.81±0.02 (R^2=0.74) for CO (Fig. 7D). For CO_2, the slope was found closer to 1.0 (1.00±0.02)

610   with an offset of -2.9±0.2 and a better R^2 (0.77) when discarding the data corresponding to the rainy season. This

611   effect is likely due to the removal of the incomplete daily time series frequently interrupted at the beginning of

612   the afternoon during the rainy season.

613   The CO_2^{ML} and CO^{ML} diurnal patterns are presented in Fig. 5A and 5B and Fig. 6A and 6B (dash lines)

614   together with those of surface measurements, after a similar filtering. The CO_2^{ML} and surface CO_2 diurnal

615   patterns (Fig. 5A and 5B) are very similar in shape and amplitude, especially during the WD, although a small

616   difference is observed at the end of the afternoon (<5 ppm). This difference is likely due to the increase of the

617   uncertainties of the MLH estimate when it is more diluted. The CO^{ML} and surface CO diurnal profiles (Fig. 6A

618   and 6B) also have similar amplitudes and shape for both WD and WE, although the CO^{ML} diurnal profile shows

619   lower values (offset around 0.1 ppm at WD). Despite this very simplified model, these results show that the total

620   column and surface measurements are mutually very consistent when the seasonal and diurnal variability of the

621   ML expansion above Mexico City is taken into account.
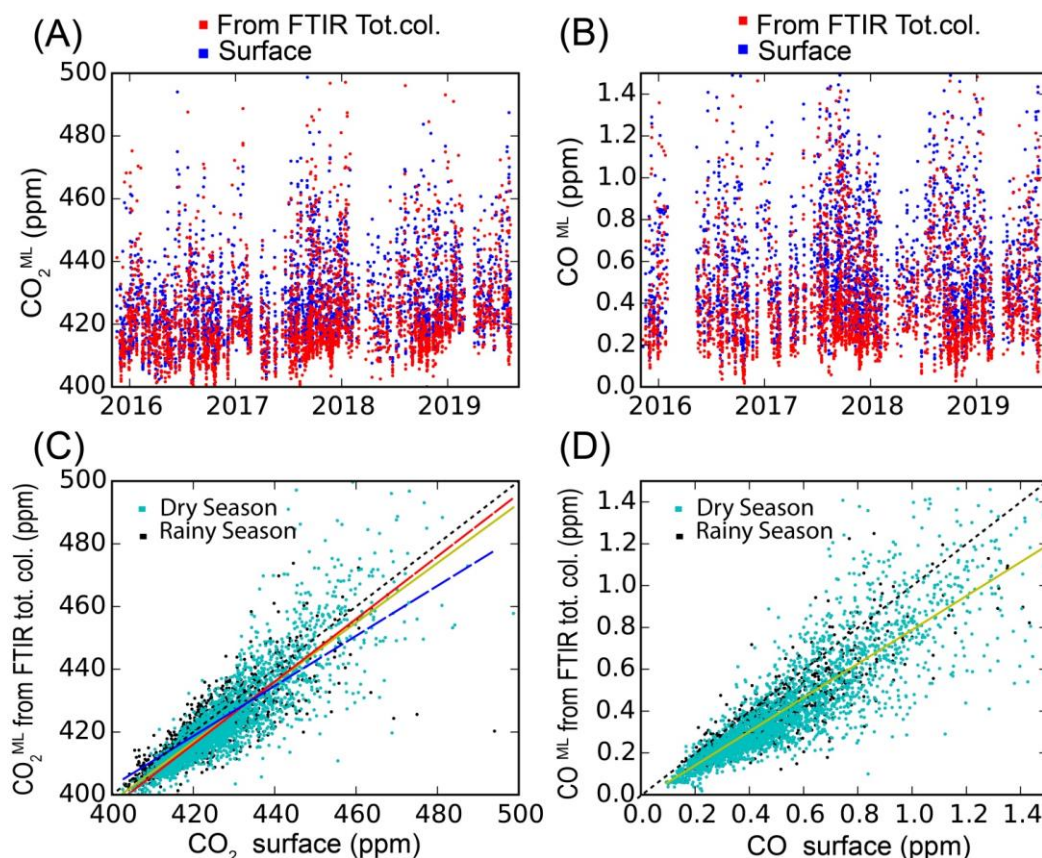
Figure 7: Comparison between (A) the CO_2^{ML} and (B) CO^{ML} products derived from the ALTZ and UNA total column measurements (red) and the surface measurements (blue) at the UNA station. (C) and (D) represent the correlation plots for CO_2 and CO, respectively. In (C) and (D), we distinguished between data corresponding to the dry (November to May: cyan) and rainy (June to October: black) seasons. In (C), yellow, red and blue linear regression curves correspond to the whole measurement period (yellow: slope=0.95±0.02; Offset= 17.9±0.2; R^2=0.74), the dry season (red: slope=1.00±0.02; Offset: -2.9±0.2; R^2=0.77) and the rainy season (blue: slope=0.80±0.03; Offset: 83.7±0.39; R^2=0.66). In (D), since no significant difference was found for the different period, the regression line (yellow: slope=0.81±0.02; offset: -0.021±0.004; R^2=0.74) represent the whole measurement. The black dash line represents y=x.

4.5 XCO$_2$ to XCO enhancements ratios

The XCO and XCO$_2$ correlated enhancements and their ratio can give insights into the combustion efficiency of the sources in a city, and therefore on their contributions. In this study we explored the variability of the XCO/XCO$_2$ ratios at both long-term and intraday scales.

For the long-term analysis, the XCO$_2$ "background" level was calculated using a statistical method, using the lower 5th percentile of the measured Xgas over a 1-day running window (You et al., 2021). We did not use the ALTZ measurements because of (i) the periodic influence of the wildfires in the region during the dry season, and (ii) the discontinuity of our daily averaged time series. The enhancements above background $\Delta_m XCO_2$ and $\Delta_m XCO$ measured at UNA and averaged by months and their ratios are presented in Fig. 8, as whisker diagrams.
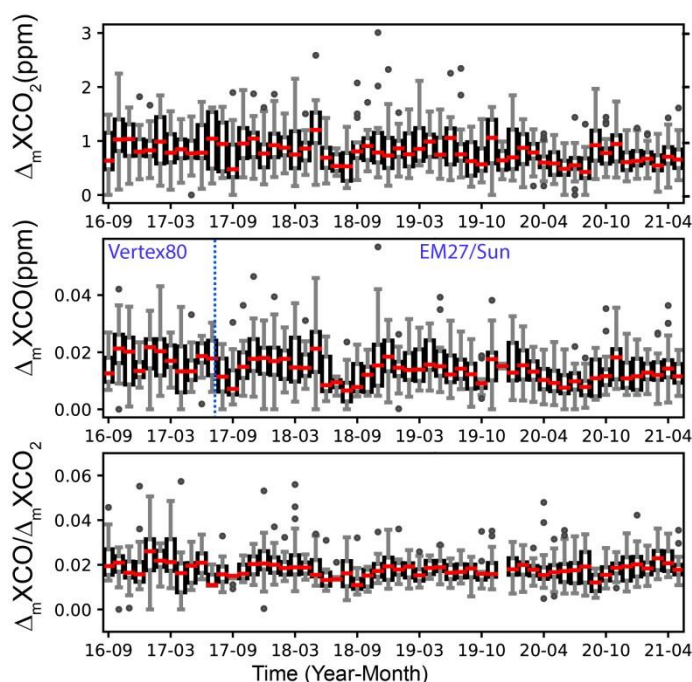
Figure 8: Whisker diagram representing by month the variability of ΔXCO₂, ΔXCO and their ratio from the UNA measurements.

Both $\Delta_m XCO_2$ and $\Delta_m XCO$ time series show a slight decrease over time (around 0.05 ppm/year and 0.001 ppm/year, respectively). Although the $\Delta_m XCO/\Delta_m XCO_2$ ratio displays a variability around its mean value (0.018±0.003), there are no discernible cyclic or long-term trend in the time series, except for the rainy periods of 2017, 2018 and 2020 when low ratios (and low $\Delta_m XCO$ and $\Delta_m XCO_2$ values) were observed. The $\Delta_m XCO$ and $\Delta_m XCO/\Delta_m XCO_2$ ratio show a higher variability at the beginning of the time series (until July 2017) likely due to the use of the CO Vertex products. The long term $\Delta_m XCO$ decrease, also observed in other studies *(*Garcia-Franco, et al., 2019; Molina, 2021, Hernández-Paniagua et al., 2021) likely reflect the effect of the successive air quality management programs implemented in the CDMX since the 1990s to improve the air quality, including technological advancements and fuel quality enhancements as well as refinery closures, industrial relocation, or fuel substitution. Regarding the low seasonal variability observed for the CO/CO_2 ratios, it is likely related to mass burning episodes and high-pressure weather conditions that occur during the dry season.

To perform the intraday analysis, the hourly-averaged data were first detrended by subtracting the daily average. The resulting ΔXCO_2 vs. ΔXCO datasets are plotted in Fig. 9A. The entire ΔXCO_2 and ΔXCO datasets showed a good correlation at both the UNA and VAL stations, with similar linear regression slopes around 0.0164±0.0003, which is consistent with that found from the surface measurements and the ML product (Fig. 9B). Although there is an actual difference in the emission types of the southern and northern parts of the city, the North hosting industrial and commercial sources and the South being largely residential and commercial, the common and dominant source of CO in the MCMA (at UNA and VAL stations) could incriminate motorised vehicles. The data dispersion around the regression line likely reflects more punctual and local influence of other sources with an important week-to-week variability.

666
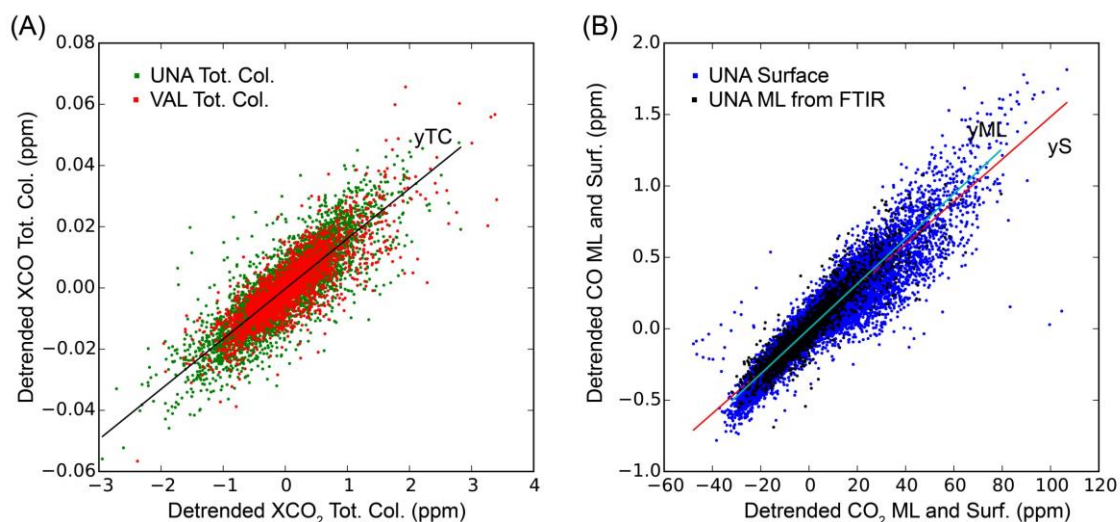
Figure 9: Correlation plot of (A) the detrended (by removing the daily averages) hourly-average total column XCO vs. XCO$_2$ data, and (B) the detrended hourly average Mixing Layer (ML) and surface CO vs. CO$_2$ products. Solid lines represent the linear regression lines, with the following parameters: TC slope=0.0164±0.0003, R^2=0.72 for the total columns at UNA and VAL; yS slope=0.0148±0.0001, R^2=0.87 for the surface products and yML slope=0.0158±0.0002, R^2=0.88 for the Mixing Layer products.

On the other hand, the total column (UNA-VAL) differences, presented in Fig. S3 can also be used to calculate the ΔXCO/ΔXCO$_2$ ratio, with a more precise subtraction of a common background (which assumes a homogeneous background across the entire city) from the two stations. Figure 10 shows the hourly-average ΔXCO$_2$ (UNA-VAL) vs. ΔXCO (UNA-VAL) correlation plot for the coincident measurement period. A well-defined linear correlation is observed with a slope of 0.015±0.001 and a coefficient of determination of R^2=0.80, highly consistent with that found in Fig. 9. The use of the (UNA-VAL) total columns difference notably improved the coefficient of determination, by removing the regional long-term and short-term perturbations affecting the two sites. The intraday variability of the ΔXCO (UNA-VAL)/ΔXCO$_2$ (UNA-VAL) ratio (Fig. 10: colour scale), showing higher columns at VAL during the morning and at UNA during the afternoon likely reflect the North to South transport of air across the city. We note that the ratio remains the same during the lock-down period. We would expect lower intraday (UNA-VAL) ΔXCO and ΔXCO$_2$ amplitudes during the lock-down period, but it is not clearly apparent in this correlation plot.
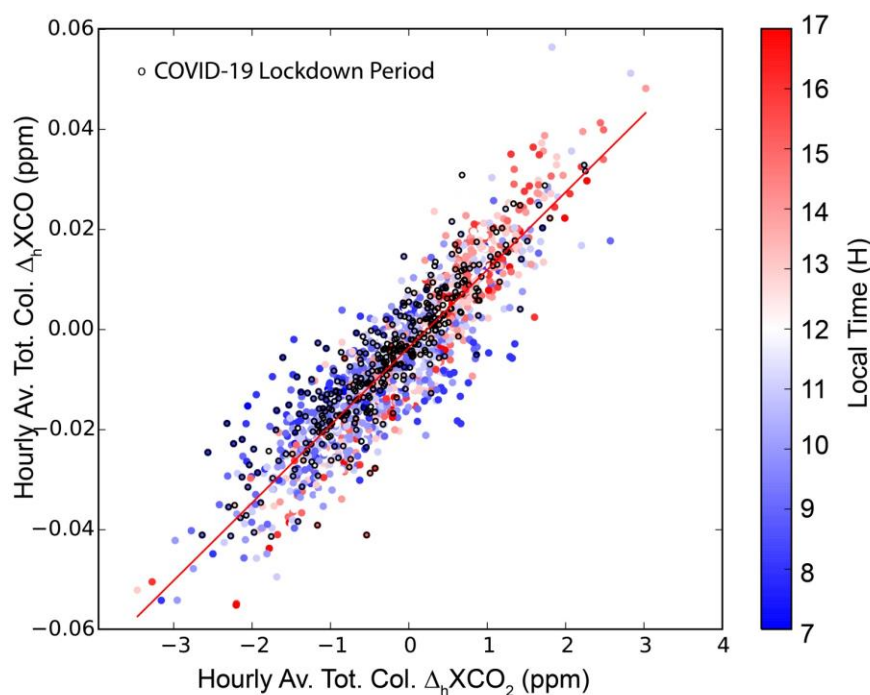
Figure 10: Correlation plot of the ΔXCO (UNA - VAL) vs. ΔXCO$_2$ (UNA - VAL) hourly averages (colour scale depending on the time is shown to the right) for the coincident measurement period (September 2019 - June 2021). Dots with black edges highlight the measurements during the COVID19 lock-down period (March-June 2020). Regression line (in red): Slope: 0.015±0.001, R^2=0.80.

4.6 Estimate of CO and CO$_2$ MCMA emissions.

The variability of the long-term CO emissions in the MCMA can be estimated, following the method detailed in Stremme et al. (2013). In that study, they assumed that, since the XCO emissions in the MCMA are mainly due to traffic pollution, the rapid changes observed in the XCO total column (less affected by the airmass vertical distribution) should reflect the CO fresh emissions under certain meteorological conditions. Low ventilation, strong turbulence in the mixed layer and limited zenithal angle of measurements are critical criteria to avoid enhancement due to horizontal transport or local heterogeneity. XCO growth rates can be estimated at specific time intervals complying with these conditions from long-term time series. Further details on the method and estimates of uncertainties due to these assumptions are given in Stremme et al. (2013). Here, we determined an optimised time interval for estimating the mean CO growth rate using (i) the diurnal surface wind speed patterns and (ii) the MLH growth rate, the latter reflecting the turbulence within the mixed layer (Fig. S4). The time interval complying with a rapid growth of the mixed layer and low surface wind speed (< 2 m.s^{-1}) was found between 10 and 12h, which is in agreement with the requirements mentioned in Stremme et al. (2013). Growth rates and their uncertainties were determined by year, based on the linear regression (with 95% confidence interval) of the 10-min averaged detrended CO total columns over the 10-12h interval. For example, for the year 2018, we found a CO growth rate of 52±5 kg.km^{-2}.h^{-1}.

To extrapolate the growth rate over the MCMA, we used the TROPOMI CO total column data that we averaged over the 2018-2022 period (Fig. 1), following the same method as described in Stremme et al. (2013). We assume that the total amount of fresh CO is proportional to the total emission of the MCMA and to the total column enhancement at the UNA site, which reflects the CO accumulated at this site. The ratio of the total accumulated CO in the MCMA to the accumulated CO at UNA is therefore the same as the emission ratio of the

710   whole Megacity to the emission flux at UNA. Therefore this ratio is the extrapolation factor and represents an

711   effective area, defined as Eq. (8):

712    $$Eff\_Area = \frac{\int (CO_{MCMA} - CO_{bgrd})}{CO_{UNA} - CO_{bgrd}}$$ (8)

713   In Eq. (8), ($CO_{MCMA} - CO_{bgrd}$) is integrated over the area where the CO TROPOMI total columns are higher than

714   a predefined background value. As the TROPOMI overflight time is around 13h30 LT, we cannot neglect the

715   ventilation and slight advection is smoothing out the distribution, so that both the background and the column at

716   UNA have to be chosen carefully. The background column was therefore estimated in two ways (i) from the

717   smallest value observed upwind of the city (cross symbol in Fig. 1) at the elevation of the Mexican basin

718   (contour line separating Mexico City from the Toluca area in the west in Fig. 1) and found to be 1.45×10^{18}

719   molec.cm^{-2} and (ii) from the Tecamac site, where the border of MCMA was assumed in Stremme et al. (2013)

720   and where the column was found to be 1.60×10^{18} molec.cm^{-2}.

721   Due to advection, even locations slightly out of the megacity are presenting enhanced CO columns and it is not

722   clear which is the background column in the Mexican basin. Figure S5 illustrated the sensitivity of the effective

723   area to the background uncertainties. A 10% higher background leads to a 40% smaller extrapolation factor and

724   a 40 % emission underestimate. The fresh CO was estimated from the TROPOMI data by removing the

725   background (1.45×10^{18} molec.cm^{-2}) to the average total columns found at UNA (1.93×10^{18} molec.cm^{-2}) and was

726   found to be 4.79×10^{17} molec.cm^{-2}. In cases where the CO total column is lower than the background, likely due

727   to the topography effect, we set the difference column to zero for the integration. This topographic effect is

728   important for the considered area, as there are plenty of mountains around the basin, like the mountain ridge in

729   the west (including Ajusco, Desierto de Leones, etc.), some mountains in the mountain ridge on the eastern part

730   of the area including in the south the two volcanoes Popocatépetl and Iztaccihuatl.

731   Finally, we found effective areas of ~2017 km^2 (outer area, blue contour line in Fig.1) and ~1178 km^2 (inner

732   area, red contour line in Fig.1) considering the two background values given above. The "inner area" reflects

733   conditions without ventilation effect, therefore the outer area is more appropriate for the emission estimates

734   given that the TROPOMI measurements occurred at 13:30 when the ventilation cannot be neglected. The other

735   estimates calculated from the inner area will be thereafter only indicated within brackets and considered to

736   estimate the sensitivity of the result.

737   Since the measured growth rate corresponds to a time interval of only 2 hours in the middle of the day, the CO

738   intraday fluctuations have to be taken into account. Stremme et al. (2013) used a factor which was taken from the

739   available bottom-up inventories and described that the CO emissions per/day are roughly 18.5 times the emission

740   per hour at noon. Assuming the same factor, we estimate a CO rate around 0.71±0.06 (0.42±0.04) Tg/year for

741   2018. If no information about the diurnal distribution of the emission rate is available, we should assume a

742   uniform distribution and an upper value of the CO rate could be estimated using an intraday time interpolation

743   factor of 24 hours instead of 18.5, finally resulting in ~30% higher estimates. Despite the significant

744   uncertainties introduced by spatial and temporal interpolation, their impact on the relative variability, trends and

745   anomalies of the emission rates is less important if the same method and assumptions are consistently applied

746   across the entire time series.

747   CO_2 emissions could not be directly estimated using the same method, given its complex diurnal pattern, which

748   is a cumulative result of both natural and anthropogenic contributions and likely been influenced by additional

749   factors, related to instrumental and retrieval effects (i.e: airmass dependence error with a sub-percentage

750   contribution for CO_2, non-ideal column sensitivity of the retrieval which represent near 25% overestimation for

751   CO_2 anomaly and 5% underestimation for CO anomaly in the PBL). Instead, we based our CO_2 estimates on the

752   measured XCO/XCO_2 ratio. The average XCO/XCO_2 molec. ratio (0.0164±0.0003) determined from the UNA

753   and VAL total column measurement (Fig. 9) was converted to a mass ratio (multiplying it by the molecular

754   weight ratio) and found to be 0.0100±0.0002. Considering this ratio, we estimated the CO_2 annual emission at

755   71±6 (42±4) Tg/year for 2018. Our estimates of CO and CO_2 emissions by year and their average over the whole

756   time series, applying the same method, are presented in Fig. 11 and Table S3, concurrently with the SEDEMA

757   inventories for the MCMA. We obtained a 2016-2021 CO and CO_2 average emissions of 0.55±0.02 (0.32±0.01)

758   and 46±2 (32±1) Tg/year, respectively, when excluding the lockdown period (Table S3). Here, the given

759   uncertainties are solely those stemming from the propagation of errors in growth rate estimates. Uncertainties on

760   absolute values are much higher when considering spatial and temporal extrapolations errors, but they do not

761   influence the interpretation of relative values.
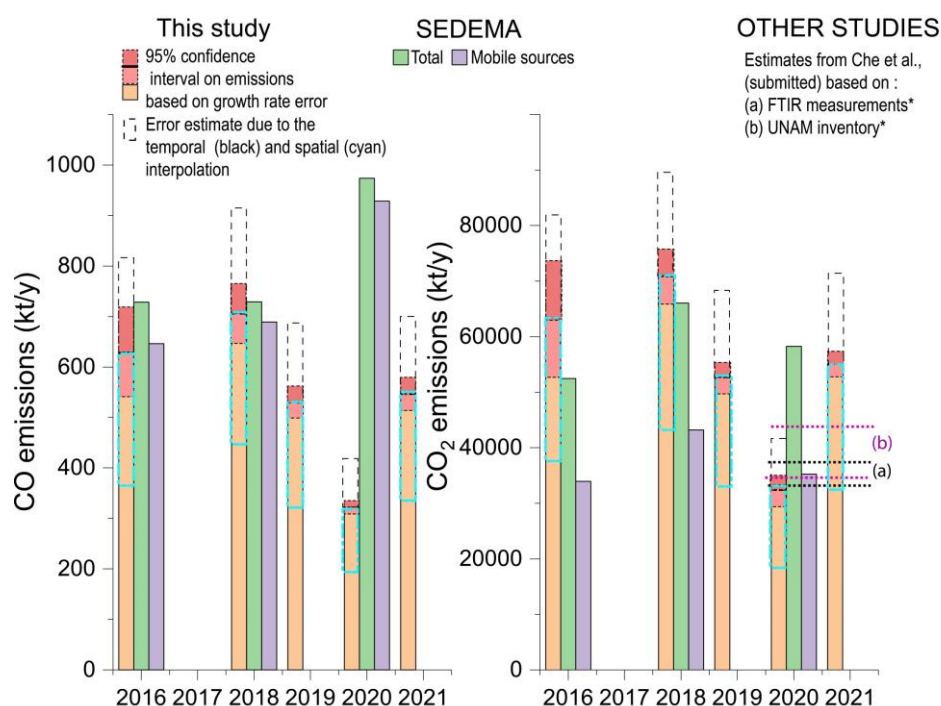
762 *: The same intraday temporal interpolation factor was applied for the comparison. (a) and (b) were based on the 10/2020 - 05/2021 period

763 **Figure 11: Comparison of CO and CO_2 emission estimates from UNA FTIR diurnal growth rates and from SEDEMA**
764 **inventories. For CO_2 (right), the estimates from Che et al. (submitted) are also reported, although it was based on the**
765 **10/2020 to 05/2021 period, after applying the same intraday temporal factor as used for our study to convert the**
766 **Gg/hour to kt/year.**

767 **5 Discussion**

768 **5.1 Long term variability**

769   In this contribution, we characterised the seasonal and inter-annual variability and trends of the CO and

770   CO_2 total column and surface concentrations from two urban and one background stations. The average total

771 column 2013-2019 growth rate obtained at ALTZ (~2.5 ppm/year) and its inter-annual variability are in
772 accordance with that typical of the Northern Hemisphere measurements from TCCON stations (hereafter, NH-
773 TCCON) (Sussman et al., 2020: AGR of 2.4 ppm/year for the 2012-2019 period).

774 Both the NH-TCCON and ALTZ stations captured an important increase of the AGR in 2016 (+1.1 ppm/year for
775 the TCCON stations and +2.1 ppm/year for the ALTZ station with respect to 2015), coinciding with the most
776 intense ENSO (El Niño Southern Oscillation) event since the 1950s'. The impact of "El Niño" events on the
777 carbon cycle is not yet fully understood, although they are consistently accompanied by a global increase of
778 XCO_2 due to increasing drought in many regions and a decrease in global land carbon uptake. In 2016, an
779 increase of 1.3 ppm/year was observed in the Mauna Loa in situ AGR with respect to 2015 (Betts et al., 2018),
780 for which the contribution of the 'El Niño' event was estimated at about 25%, the rest ascribed to an increase of
781 the anthropogenic emissions. In Mexico, the "El Niño" events are generally associated with a decrease in
782 precipitations, with deficits which can reach up to 250 mm in the South-Western area of the country, causing
783 drought and a higher occurrence of wild and forest fires (Bravo-Cabrera et al., 2018, González del Castillo et al.,
784 2020). Our observations from the ALTZ measurements highlight a much higher XCO_2 increase (+2.1 ppm/year)
785 during 2016 with respect to 2015 than that observed at the NH-TCCON stations. During this period a small
786 increase in the XCO MAGR (~ +0.02 ppm) is also observed at both ALTZ and UNA stations, maintaining the
787 highest values of the whole time series over more than 4 months. Assuming that the CO MAGR variability
788 captured at the ALTZ station during 2016 rather reflects a change in the global MCMA's emissions, we attempt
789 to delineate the global and local contributions in the 2016 XCO_2 ALTZ AGR increase. Adopting a molecular
790 CO/CO_2 ratio of ~ 0.016, a hypothetical increase of the XCO_2 MAGR over the 09/2015 - 09/2016 period due to
791 the local emissions would be around +1.2 ppm/year, thus about 60% of the observed increasing rate during this
792 period (+2.1 ppm/year). This gross estimate suggests that the El Niño regional effect only contributed at about
793 25% (0.9 ppm) to the observed AGR increase, which is close to the estimate from the NH-TCCON stations (~
794 +1.1 ppm) and from in situ data.

795 On the other hand, our long-term FTIR and surface time series allows examining the effect of the COVID-19
796 lock-down on the tropospheric CO_2 and CO concentration above the MCMA at local and regional scales. The
797 reduction of the surface CO and CO_2 AGR at UNA (CO_2 AGR to a value close to zero, and CO AGR ~ -0.1
798 ppm/year) with respect to the other years (Fig. 3), and the strong diminution of their amplitude in the mean
799 diurnal cycles clearly reflect a significant decrease of the local emissions near the UNA station, likely due to a
800 drastic reduction of the urban traffic (the average annual congestion level decreased from 52% in 2019 to 36% in
801 2020 in Mexico City, from TomTom available estimates https://www.tomtom.com/traffic-index/mexico-city-
802 traffic/).

803 The FTIR total column XCO_2 and XCO time series at UNA did not capture such a drastic change, only a small
804 punctual decrease of the MAGR lower than the standard deviation of the whole time series was observed
805 between April and October 2020. These results are in accordance with previous studies in other parts of the
806 world. Although a reduction of 8.8% of the global CO_2 emissions was observed during the first five months of
807 2020 (Liu et al., 2020; Jones et al., 2020) and an annual reduction from 4 to 7% (Le Quéré et al., 2020), the
808 atmospheric total column XCO_2 showed a less clear effect (Sussman et al., 2020).

5.2 CO/CO$_2$ ratio and MCMA emission estimates

In this study, we robustly determined the CO/CO$_2$ ratio characterising the combustion efficiency of the city (0.016±0.01) from both surface and total column measurements at two urban stations. We found the same ratio for the UNA and VAL stations, and this ratio is very consistent with that found using the (UNA-VAL) gradients and using the surface measurements. This ratio is also consistent with that reported by MacDonald et al. (2023), calculated from TROPOMI and OCO-2/3 measurements (0.019) and slightly higher than that obtained from the EDGAR, FFDAS and ODIAC inventories (ratio ~0.012) reported in the same study.

Our estimate of CO emissions from the UNA measurements is based on a simplified approach, limited to days with low ventilation and time intervals corresponding to the late morning hours. It assumes a homogeneous area in the footprint and averages selected days without discrimination. Given that the temporal and spatial extrapolation introduces large uncertainties, only the relative and interannual behaviour of the emission can be discussed here, but the approach demonstrates how close column growth rate can be related to emission flux, if meteorological conditions allow neglecting advection. Our estimated range of CO emissions are consistent with the SEDEMA inventories at least for the year 2016 (factor 0.98) and 2018 (factor 1.04) if considering that they are dominated by the mobile sources. However, it is not the case for 2020, for which our estimate is much lower than SEDEMA by a factor of 0.3. During the lock-down period we estimated a decrease of about 55% compared to 2018 while in the SEDEMA report, 2020 is the year with the maximum CO emissions (increase of 35% compared to 2018 considering the mobile sources). Both of these estimates contrast with Kutralam-Muniasamy et al. (2021), which reported an increase of 1.1% during the lock-down using the RAMA surface data. The large difference observed between these different studies can be due to i) the different methods used for extrapolating in space and time the emissions, ii) higher uncertainties of the FTIR-based estimates due to an important reduction the selected days of measurements and iii) an over-estimation of the SEDEMA inventory due to a lack of data during the lock-down period. Our estimate is based on the extrapolation of data from only one station (UNA), for which the dominant source is mainly the UNAM traffic activity. During the lockdown, the UNAM was closed and a significant reduction of the local traffic was recorded, but this traffic reduction was likely not representative of the whole MCMA. However, the decrease of the MAGR at both VAL and UNA stations does not support the increase of the CO emissions estimated by the SEDEMA inventory. Interestingly, it was not possible to apply the same method to calculate CO emissions at VAL because the average growth rate was close to zero (Fig. 6). This behaviour at VAL is likely due to the fast dispersion of the pollutant at this site, weakening the link between the diurnal pattern and the emissions.

Regarding CO$_2$, our estimates also agree with the SEDEMA's inventory, especially if we consider the total emissions instead of mobile sources (factor of 1.2 and 1.1) for the years 2016 and 2018. For 2020, we estimated a decrease of 55% while the SEDEMA inventory indicates a decrease of about 10%. The CO/CO$_2$ ratios calculated from the SEDEMA data for total emissions are similar to ours (0.014 and 0.011 in 2016 and 2018, respectively), suggesting that our average CO/CO$_2$ ratio is actually representative of the global mixing of the different sources of the MCMA, and not only dominated by the road traffic. Interestingly, according to the SEDEMA inventory, road traffic, the main anthropogenic CO source is identified by ratios (0.019 and 0.016 in 2016 and 2018, respectively) only slightly higher than our global average; whilst the industrial and domestic burning sectors, which represent the second main CO$_2$ anthropogenic sources, produces a one order of magnitude lower ratio. In any case, our measurements are well representative of the main source of the CO and CO$_2$

849 anthropogenic emissions. Indeed, if we consider the 2018 SEDEMA ratio for mobile sources (0.016), we find

850 CO_2 emissions of the order of 43,100 kt/year for this year, within ~5% of the SEDEMA estimates.

851 Our results were also compared with the estimates reported in Che et al. (submitted), Che et al. (2023) and

852 Grutter et al. (2024) based on an intensive FTIR measurement campaign performed during the 10/2020 to

853 05/2021 period and using a Column-Stochastic Time-Inverted Lagrangian Transport model (X-STILT) and a

854 bayesian inversion (Fig. 11). Considering the same measurement period, our method leads to CO_2 emission

855 estimates ranging between 29,000 and 49,800 kt/year using inner and outer effective area, respectively, which is

856 consistent with the estimates obtained in Che et al. (submitted), ranging between 32,700 and 37,200 kt/year

857 when applying the same intraday temporal extrapolation factor. Although the method we used for estimating the

858 MCMA emissions is coarse and contains large uncertainties, mainly due to the temporal and space extrapolation,

859 it shows the ability to use one station capturing the variability of the anthropogenic emissions of the MCMA and

860 providing a year-by-year follow-up emission information without using complex dispersion models.

861 **6 Summary and conclusion**

862 We have analysed the variability of the total column XCO and XCO_2 above the MCMA from two urban

863 and one background stations. The long-term XCO_2 data at the ALTZ station shows an average annual growth

864 rate of ~2.5 ppm/year, similar to what has been reported from TCCON stations in the northern hemisphere, and

865 captured the perturbation driven by the 2015-2016 El Niño event. The urban stations show a similar growth rate

866 (~2.3 ppm/year) and unlike at ALTZ, a slight decrease of XCO_2 and XCO during the COVID19 lock-down

867 period could be observed. The CO_2 and CO concentrations within the mixed layer, estimated from the FTIR total

868 column measurements and ceilometer data, were found to be consistent with the surface measurements. These

869 findings confirm that the concentrations near the surface are mainly controlled by the emissions and the daily

870 behaviour of the mixed layer in MCMA. Our long-term total column and surface time series from both urban

871 stations allowed us to determine with great confidence an average CO/CO_2 ratio, indicative of the Mexico City

872 combustion efficiency. The CO/CO_2 ratio over our long-term measurement period seems to be fairly constant

873 and equals ~0.016 (mass ratio: 0.010). This value is consistent with other studies such as from satellite

874 measurements (OCO-2/3 and TROPOMI) and the bottom-up inventories reported by MacDonald et al. (2023).

875 Finally, we estimated the CO emissions using the average daily growth rate determined from measurements at

876 the UNA station. Although this method likely leads to an under-estimate of the emissions due to the non-

877 negligible effects of advection, our results were found to be very consistent with the 2016 and 2018 SEDEMA

878 inventories. The same strategy could not be applied at the VAL station, likely because of dominant southward

879 advection of the airmass, due to the complex topography in this part of the MCMA. In contrast, the UNA station

880 is located in a flat ground downwind of the main anthropogenic source of the MCMA which likely allows

881 establishing a direct relationship between the columnar measurements and the MCMA CO and CO_2 emissions.

882 We finally estimated the CO_2 emissions using the CO growth rate and the CO/CO_2 ratio. The finding that our

883 CO_2 emission estimates are within 20% of those of SEDEMA for total emissions show that our ratio reflects not

884 only the traffic sources but is also affected by other sources such as industrial activities and domestic burning.

885 The UNA station, with its advantageous orography, is therefore a good site to capture well-mixed emissions

886 from the city and serves as a site to follow the interannual variability and trends of the emissions in this urban

887 environment. Finally, this study showed the feasibility to monitor the long-term evolution of anthropogenic CO_2

888   and CO emissions in Mexico City by deploying only a few EM27/SUN instruments. The methodology employed
889   here for monitoring the long-term temporal variability of CO emission fluxes is likely to be adapted to other
890   urban areas where the topography damps the ventilation down for several hours each day, thereby establishing
891   that the column growth rate is dominated by the emission flux. Although the straightforward model presented
892   here is not intended to replace a complex transport/chemical model for a precise estimate of city emissions, the
893   results obtained demonstrate that it is nevertheless possible to track their temporal evolution with a high degree
894   of reliability.

895   **7 Author contribution**

896   All the co-authors contributed in the discussion of concepts, and to the preparation of the manuscript. NT, WS
897   and MG were responsible of FTIR measurements and the data analysis. MG and WS lead the ALTZ station
898   development and its long-term operation. AB and EGC were responsible of the maintenance of the instruments
899   at the Altzomoni station. VA helped to classify the days and hours with low ventilation and strong turbulence
900   and provided the UNAM emission inventory. EGC was in charge of the in-situ measurements, with the support
901   of OL. MG and MR led the MERCI-CO2 project. FH lead at KIT the German-Mexican collaboration for the
902   deployment of the high resolution FTIR spectrometer and supports its long-term operation as part of NDACC.
903   FH has helped in the design and setup of the spectrometer and solar tracker before it was shipped to Mexico. He
904   has developed the retrieval code PROFFIT and gives continuously support to the UNAM group for its use and in
905   operating the spectrometer. FH and CA lead the German-Mexican collaboration and give precious help for the
906   EM27/Sun measurements in the frame of the COCCON network. All the co-authors contributed of the writing of
907   the manuscript.

908   **8 Competing interests**

909   The authors declare that they have no conflict of interest.

910   **9 Acknowledgements**

911   We thank the two reviewers for their very constructive comments, which help to significantly improve the
912   manuscript. We acknowledge the CONACyT-ANR project 290589 'Mexico City's Regional Carbon Impacts'
913   (ANR-17-CE04-0013-01) for funding. Also the former projects CONACYT 239618 "El estudio del ciclo de
914   Carbono y de los gases de efecto invernadero utilizando espectroscopia de absorción solar" and UNAM-DGAPA
915   PAPIIT IN111521/IN106024 are acknowledged. We acknowledge the technical assistance provided by Omar
916   López, Alfredo Rodriguez, Miguel Robles, Delibes Flores, and the Instituto de Ciencias de la Atmósfera y del
917   Cambio Climatico (UNAM) for the institutional support to carry out this study. We thank T. Blumenstock from
918   the KIT for his precious help and fruitful discussion during the last years. We thank Dr. Thomas Boulesteix for
919   his help at the Altzomoni site, his fruitful discussions.

920

10 References

Alberti Arroyo, C. A.: Ground based FTIR and MAX-DOAS observations of greenhouse and trace gas emissions in the Rhine valley (Germany), St. Petersburg and Yekaterinburg (Russia), Karlsruher Institut für Technologie (KIT), https://doi.org/10.5445/IR/1000162056/v2, 2023.

Alberti, C., Hase, F., Frey, M., Dubravica, D., Blumenstock, T., Dehn, A., Castracane, P., Surawicz, G., Harig, R., Baier, B. C., Bès, C., Bi, J., Boesch, H., Butz, A., Cai, Z., Chen, J., Crowell, S. M., Deutscher, N. M., Ene, D., Franklin, J. E., García, O., Griffith, D., Grouiez, B., Grutter, M., Hamdouni, A., Houweling, S., Humpage, N., Jacobs, N., Jeong, S., Joly, L., Jones, N. B., Jouglet, D., Kivi, R., Kleinschek, R., Lopez, M., Medeiros, D. J., Morino, I., Mostafavipak, N., Müller, A., Ohyama, H., Palmer, P. I., Pathakoti, M., Pollard, D. F., Raffalski, U., Ramonet, M., Ramsay, R., Sha, M. K., Shiomi, K., Simpson, W., Stremme, W., Sun, Y., Tanimoto, H., Té, Y., Tsidu, G. M., Velazco, V. A., Vogel, F., Watanabe, M., Wei, C., Wunch, D., Yamasoe, M., Zhang, L., and Orphal, J.: Improved calibration procedures for the EM27/SUN spectrometers of the COllaborative Carbon Column Observing Network (COCCON), Atmospheric Measurement Techniques, 15, 2433–2463, https://doi.org/10.5194/amt-15-2433-2022, 2022.

Babenhauserheide, A., Hase, F., and Morino, I.: The Fossil Fuel Emissions of Tokyo estimated directly from measurements of the Tsukuba TCCON site, Gases/Remote Sensing/Data Processing and Information Retrieval, https://doi.org/10.5194/amt-2018-224, 2018.

Baylon, J. L., Stremme, W., Grutter, M., Hase, F., and Blumenstock, T.: Background CO_2 levels and error analysis from ground-based solar absorption IR measurements in central Mexico, Atmos. Meas. Tech., 10, 2425–2434, https://doi.org/10.5194/amt-10-2425-2017, 2017.

Betts, R. A., Jones, C. D., Knight, Jeff. R., Keeling, Ralph. F., Kennedy, John. J., Wiltshire, A. J., Andrew, R. M., and Aragão, L. E. O. C.: A successful prediction of the record CO_2 rise associated with the 2015/2016 El Niño, Phil. Trans. R. Soc. B, 373, 20170301, https://doi.org/10.1098/rstb.2017.0301, 2018.

Bezanilla, A., Krüger, A., Stremme, W., and Grutter, M.: Solar absorption infrared spectroscopic measurements over Mexico City: Methane enhancements, Atmósfera, 27, 173–183, https://doi.org/10.1016/S0187-6236(14)71108-7, 2014.

Borsdorff, T., Hasekamp, O. P., Wassmann, A., and Landgraf, J.: Insights into Tikhonov regularization: application to trace gas column retrieval and the efficient calculation of total column averaging kernels, Atmos. Meas. Tech., 7, 523–535, https://doi.org/10.5194/amt-7-523-2014, 2014.

Borsdorff, T., Aan de Brugh, J., Hu, H., Aben, I., Hasekamp, O., and Landgraf, J.: Measuring Carbon Monoxide With TROPOMI: First Results and a Comparison With ECMWF-IFS Analysis Data, Geophysical Research Letters, 45, 2826–2832, https://doi.org/10.1002/2018GL077045, 2018.

Borsdorff, T., García Reynoso, A., Maldonado, G., Mar-Morales, B., Stremme, W., Grutter, M., and Landgraf, J.: Monitoring CO emissions of the metropolis Mexico City using TROPOMI CO observations, Atmos. Chem. Phys., 20, 15761–15774, https://doi.org/10.5194/acp-20-15761-2020, 2020.

Bravo Cabrera, J. L., Azpra Romero, E., Rodriguez Gonzalez, F. J., and Rodriguez López, O.: Effects of ENSO on precipitation in Mexico City, Investigaciones Geográficas, https://doi.org/10.14350/rig.59679, 2018.

Buchwitz, M., Reuter, M., Schneising, O., Noël, S., Gier, B., Bovensmann, H., Burrows, J. P., Boesch, H., Anand, J., Parker, R. J., Somkuti, P., Detmers, R. G., Hasekamp, O. P., Aben, I., Butz, A., Kuze, A., Suto, H., Yoshida, Y., Crisp, D., and O'Dell, C.: Computation and analysis of atmospheric carbon dioxide annual mean growth rates from satellite observations during 2003–2016, Atmos. Chem. Phys., 18, 17355–17370, https://doi.org/10.5194/acp-18-17355-2018, 2018.

Burgos-Cuevas, A., Magaldi, A., Adams, D. K., Grutter, M., García Franco, J. L., and Ruiz-Angulo, A.: Boundary Layer Height Characteristics in Mexico City from Two Remote Sensing Techniques, Boundary-Layer Meteorol, 186, 287–304, https://doi.org/10.1007/s10546-022-00759-w, 2023.

Che, K., Cai, Z., Liu, Y., Wu, L., Yang, D., Chen, Y., Meng, X., Zhou, M., Wang, J., Yao, L., and Wang, P.: Lagrangian inversion of anthropogenic CO_2 emissions from Beijing using differential column measurements, Environ. Res. Lett., 17, 075001, https://doi.org/10.1088/1748-9326/ac7477, 2022.

Che, K., Lauvaux, T., Taquet, N., Stremme, W., Xu, Y., Alberti, C., Lopez, M., García-Reynoso, A., Ciais, P., Liu,Y., Ramonet, M., Grutter, M. (2024). CO2 emissions estimate from Mexico City using ground- and space-based remote sensing. submitted to Journal of Geophysical Research.

Che, K., Lauvaux, T., Taquet, N., Stremme, W., Xu, Y., Alberti, C., Lopez, M., García-Reynoso, A., Ciais, P., Liu,Y., Ramonet, M., Grutter, M. (2024). Urban XCO2 gradients from a dense network of solar absorption spectrometers and OCO-3 over Mexico City. Journal of Geophysical Research: Atmospheres, 129(9), e2023JD040063.,https://doi.org/10.1029/2023JD040063

Che, K., Lauvaux, T., Taquet, N., Xu, Y., Lopez, M., Stremme, W., García-Reynoso, A., Ciais, P., Liu, Y., Ramonet, M., and Grutter, M.: CO2 emissions estimate from Mexico City using ground- and space-based remote sensing, , https://doi.org/10.5194/egusphere-egu23-16636, 2023.

Chen, J., Viatte, C., Hedelius, J. K., Jones, T., Franklin, J. E., Parker, H., Gottlieb, E. W., Wennberg, P. O., Dubey, M. K., and Wofsy, S. C.: Differential column measurements using compact solar-tracking spectrometers, Atmos. Chem. Phys., 16, 8479–8498, https://doi.org/10.5194/acp-16-8479-2016, 2016.

Chevallier, F., Deutscher, N. M., Conway, T. J., Ciais, P., Ciattaglia, L., Dohe, S., Fröhlich, M., Gomez-Pelaez, A. J., Griffith, D., Hase, F., Haszpra, L., Krummel, P., Kyrö, E., Labuschagne, C., Langenfelds, R., Machida, T., Maignan, F., Matsueda, H., Morino, I., Notholt, J., Ramonet, M., Sawa, Y., Schmidt, M., Sherlock, V., Steele, P., Strong, K., Sussmann, R., Wennberg, P., Wofsy, S., Worthy, D., Wunch, D., and Zimnoch, M.: Global CO_2 fluxes inferred from surface air-sample measurements and from TCCON retrievals of the CO_2 total column: TWO CO_2 FLUX INVERSIONS, Geophys. Res. Lett., 38, n/a-n/a, https://doi.org/10.1029/2011GL049899, 2011.

de Foy, B., Varela, J. R., Molina, L. T., and Molina, M. J.: Rapid ventilation of the Mexico City basin and regional fate of the urban plume, Atmos. Chem. Phys., 6, 2321–2335, https://doi.org/10.5194/acp-6-2321-2006, 2006.

Duren, R. M. and Miller, C. E.: Measuring the carbon emissions of megacities, Nature Clim Change, 2, 560–562, https://doi.org/10.1038/nclimate1629, 2012.

Frey, M., Sha, M. K., Hase, F., Kiel, M., Blumenstock, T., Harig, R., Surawicz, G., Deutscher, N. M., Shiomi, K., Franklin, J. E., Bösch, H., Chen, J., Grutter, M., Ohyama, H., Sun, Y., Butz, A., Mengistu Tsidu, G., Ene, D., Wunch, D., Cao, Z., Garcia, O., Ramonet, M., Vogel, F., and Orphal, J.: Building the COllaborative Carbon Column Observing Network (COCCON): long-term stability and ensemble performance of the EM27/SUN Fourier transform spectrometer, Atmos. Meas. Tech., 12, 1513–1530, https://doi.org/10.5194/amt-12-1513-2019, 2019.

Frey, M. M., Hase, F., Blumenstock, T., Dubravica, D., Groß, J., Göttsche, F., Handjaba, M., Amadhila, P., Mushi, R., Morino, I., Shiomi, K., Sha, M. K., De Mazière, M., and Pollard, D. F.: Long-term column-averaged greenhouse gas observations using a COCCON spectrometer at the high-surface-albedo site in Gobabeb, Namibia, Atmos. Meas. Tech., 14, 5887–5911, https://doi.org/10.5194/amt-14-5887-2021, 2021.

García-Franco, J. L., Stremme, W., Bezanilla, A., Ruiz-Angulo, A., and Grutter, M.: Variability of the Mixed-Layer Height Over Mexico City, Boundary-Layer Meteorol, 167, 493–507, https://doi.org/10.1007/s10546-018-0334-x, 2018.

García-Franco, J. L.: Air quality in Mexico City during the fuel shortage of January 2019. Atmospheric environment, 222, 117131, 2020.

Gisi, M.: Setup of precise camera based solar tracker systems and greenhouse gas measurements using a modified portable spectrometer, https://doi.org/10.5445/IR/1000031248, 2012.

Gisi, M., Hase, F., Dohe, S., and Blumenstock, T.: Camtracker: a new camera controlled high precision solar tracker system for FTIR-spectrometers, Atmos. Meas. Tech., 4, 47–54, https://doi.org/10.5194/amt-4-47-2011, 2011.

Gisi, M., Hase, F., Dohe, S., Blumenstock, T., Simon, A., and Keens, A.: XCO2 measurements with a tabletop FTS using solar absorption spectroscopy, Atmos. Meas. Tech., 5, 2969–2980, https://doi.org/10.5194/amt-5-2969-2012, 2012.

Goldberg, D. L., Lu, Z., Oda, T., Lamsal, L. N., Liu, F., Griffin, D., McLinden, C. A., Krotkov, N. A., Duncan, B. N., and Streets, D. G.: Exploiting OMI NO2 satellite observations to infer fossil-fuel CO2 emissions from U.S. megacities, Science of The Total Environment, 695, 133805, https://doi.org/10.1016/j.scitotenv.2019.133805, 2019.

González Del Castillo, E., Taquet, N., Bezanilla, A., Stremme, W., Ramonet, M., Laurent, O, Xu, Y., Delmotte, M., Grutter, M.: CO2 variability in the Mexico City region from in situ measurements at an urban and a background site, Atm., 35, 377–393, https://doi.org/10.20937/ATM.52956, 2022.

Grutter, M.: Multi-Gas analysis of ambient air using FTIR spectroscopy over Mexico City, Atmosfera, 16, 1–13, 2003.

Grutter, M., Rivera, O., Retama, A., Contreras, J., González, E., Porras, S., López, O., Arredondo, T., Díaz, A., Robles, M., Sánchez B., Azpra, E., Ladino, L. Technical Report #4 in "EVALUACIÓN DE DISPOSITIVOS BASADOS EN MICROSENSORES PARA EL MONITOREO CONTINUO DE LA CALIDAD DEL AIRE", ICAyCC-UNAM 2023.

Grutter, M., Flores, E., Basaldud, R., & Ruiz-Suárez, L. G. (2003). Open-path FTIR spectroscopic studies of the trace gases over Mexico City. *ATMOSPHERIC AND OCEANIC OPTICS C/C OF OPTIKA ATMOSFERY I OKEANA*, *16*(3), 232-236.

Grutter, M., Ramonet, M., Lauvaux, T., Che, K., Taquet, N., Stremme, W., Alberti, C., Almanza, V., Bezanilla, A., Ciais, P., García-Reynoso, A., González, E., Hase, F., Xu, Y., Laurent, O., Lopez, M., Liu, Y., Porras, S., Xu, Y. (2024). NDACC/IRWG-TCCON-COCCON Annual Meeting 2024, available at https://tccon-wiki.caltech.edu/pub/Main/2024Boulder/5.Grutter_Mexico_City.pdf

Gurney, K. R., Liang, J., O'Keeffe, D., Patarasuk, R., Hutchins, M., Huang, J., Rao, P., and Song, Y.: Comparison of Global Downscaled Versus Bottom-Up Fossil Fuel CO_2 Emissions at the Urban Scale in Four U.S. Urban Areas, JGR Atmospheres, 124, 2823–2840, https://doi.org/10.1029/2018JD028859, 2019.

Hakkarainen, J., Szeląg, M. E., Ialongo, I., Retscher, C., Oda, T., and Crisp, D.: Analyzing nitrogen oxides to carbon dioxide emission ratios from space: A case study of Matimba Power Station in South Africa, Atmospheric Environment: X, 10, 100110, https://doi.org/10.1016/j.aeaoa.2021.100110, 2021.

Hardy, C. C.: Smoke management guide for prescribed and wildland fire, National Wildlife Coordinating Group, 2001.

Hase, F., Hannigan, J. W., Coffey, M. T., Goldman, A., Höpfner, M., Jones, N. B., Rinsland, C. P., and Wood, S. W.: Intercomparison of retrieval codes used for the analysis of high-resolution, ground-based FTIR measurements, Journal of Quantitative Spectroscopy and Radiative Transfer, 87, 25–52, https://doi.org/10.1016/j.jqsrt.2003.12.008, 2004.

Hase, F., Frey, M., Blumenstock, T., Groß, J., Kiel, M., Kohlhepp, R., Mengistu Tsidu, G., Schäfer, K., Sha, M. K., and Orphal, J.: Application of portable FTIR spectrometers for detecting greenhouse gas emissions of the major city Berlin, Atmos. Meas. Tech., 8, 3059–3068, https://doi.org/10.5194/amt-8-3059-2015, 2015.

Hase, F., Frey, M., Kiel, M., Blumenstock, T., Harig, R., Keens, A., and Orphal, J.: Addition of a channel for XCO observations to a portable FTIR spectrometer for greenhouse gas measurements, Atmospheric Measurement Techniques, 9, 2303–2313, 2016.

Hedelius, J. K., Viatte, C., Wunch, D., Roehl, C. M., Toon, G. C., Chen, J., Jones, T., Wofsy, S. C., Franklin, J. E., Parker, H., Dubey, M. K., and Wennberg, P. O.: Assessment of errors and biases in retrievals of XCO_2, XCH_4, XCO, and XN_2O from a 0.5 cm−1 resolution solar-viewing spectrometer, Atmos. Meas. Tech., 9, 3527–3546, https://doi.org/10.5194/amt-9-3527-2016, 2016.

Hedelius, J. K., Liu, J., Oda, T., Maksyutov, S., Roehl, C. M., Iraci, L. T., Podolske, J. R., Hillyard, P. W., Liang, J., Gurney, K. R., Wunch, D., and Wennberg, P. O.: Southern California megacity CO_2, CH_4, and CO flux estimates using ground- and space-based remote sensing and a Lagrangian model, Atmos. Chem. Phys., 18, 16271–16291, https://doi.org/10.5194/acp-18-16271-2018, 2018.

Hernández-Paniagua, I. Y., Valdez, S. I., Almanza, V., Rivera-Cárdenas, C., Grutter, M., Stremme, W., García Reynoso, A., Ruiz-Suárez, L. G. (2021). Impact of the COVID-19 lockdown on air quality and resulting public health benefits in the Mexico City metropolitan area. Frontiers in public health, 9, 642630.

Herrera, B., Bezanilla, A., Blumenstock, T., Dammers, E., Hase, F., Clarisse, L., Magaldi, A., Rivera, C., Stremme, W., Strong, K., Viatte, C., Van Damme, M., and Grutter, M.: Measurement report: Evolution and distribution of NH_3 over Mexico City from ground-based and satellite infrared spectroscopic measurements, Atmos. Chem. Phys., 22, 14119–14132, https://doi.org/10.5194/acp-22-14119-2022, 2022.

Hersbach, H., Bell, B., Berrisford, P., Hirahara, S., Horányi, A., Muñoz-Sabater, J., Nicolas, J., Peubey, C., Radu, R., Schepers, D., Simmons, A., Soci, C., Abdalla, S., Abellan, X., Balsamo, G., Bechtold, P., Biavati, G., Bidlot, J., Bonavita, M., De Chiara, G., Dahlgren, P., Dee, D., Diamantakis, M., Dragani, R., Flemming, J., Forbes, R., Fuentes, M., Geer, A., Haimberger, L., Healy, S., Hogan, R. J., Hólm, E., Janisková, M., Keeley, S., Laloyaux, P., Lopez, P., Lupu, C., Radnoti, G., De Rosnay, P., Rozum, I., Vamborg, F., Villaume, S., and Thépaut, J.: The ERA5 global reanalysis, Quart J Royal Meteoro Soc, 146, 1999–2049, https://doi.org/10.1002/qj.3803, 2020.

Jones, C. D., Hickman, J. E., Rumbold, S. T., Walton, J., Lamboll, R. D., Skeie, R. B., Fiedler, S., Forster, P. M., Rogelj, J., Abe, M., Botzet, M., Calvin, K., Cassou, C., Cole, J. N. S., Davini, P., Deushi, M., Dix, M., Fyfe, J. C., Gillett, N. P., Ilyina, T., Kawamiya, M., Kelley, M., Kharin, S., Koshiro, T., Li, H., Mackallah, C., Müller, W. A., Nabat, P., Van Noije, T., Nolan, P., Ohgaito, R., Olivié, D., Oshima, N., Parodi, J., Reerink, T. J., Ren, L., Romanou, A., Séférian, R., Tang, Y., Timmreck, C., Tjiputra, J., Tourigny, E., Tsigaridis, K., Wang, H., Wu, M., Wyser, K., Yang, S., Yang, Y., and Ziehn, T.: The Climate Response to Emissions Reductions Due to COVID-19: Initial Results From CovidMIP, Geophysical Research Letters, 48, e2020GL091883, https://doi.org/10.1029/2020GL091883, 2021.

Kiel, M., Eldering, A., Roten, D. D., Lin, J. C., Feng, S., Lei, R., Lauvaux, T., Oda, T., Roehl, C. M., Blavier, J.-F., and Iraci, L. T.: Urban-focused satellite CO2 observations from the Orbiting Carbon Observatory-3: A first look at the Los Angeles megacity, Remote Sensing of Environment, 258, 112314, https://doi.org/10.1016/j.rse.2021.112314, 2021.

Kutralam-Muniasamy, G., Pérez-Guevara, F., Roy, P. D., Elizalde-Martínez, I., and Shruti, V. C.: Impacts of the COVID-19 lockdown on air quality and its association with human mortality trends in megapolis Mexico City, Air Qual Atmos Health, 14, 553–562, https://doi.org/10.1007/s11869-020-00960-1, 2021.

Le Quéré, C., Jackson, R. B., Jones, M. W., Smith, A. J. P., Abernethy, S., Andrew, R. M., De-Gol, A. J., Willis, D. R., Shan, Y., Canadell, J. G., Friedlingstein, P., Creutzig, F., and Peters, G. P.: Temporary reduction in daily global CO2 emissions during the COVID-19 forced confinement, Nat. Clim. Chang., 10, 647–653, https://doi.org/10.1038/s41558-020-0797-x, 2020.

Lei, R., Feng, S., Danjou, A., Broquet, G., Wu, D., Lin, J. C., O'Dell, C. W., and Lauvaux, T.: Fossil fuel CO_2 emissions over metropolitan areas from space: A multi-model analysis of OCO-2 data over Lahore, Pakistan, Remote Sensing of Environment, 264, 112625, https://doi.org/10.1016/j.rse.2021.112625, 2021.

Lian, J., Lauvaux, T., Utard, H., Bréon, F.-M., Broquet, G., Ramonet, M., Laurent, O., Albarus, I., Chariot, M., Kotthaus, S., Haeffelin, M., Sanchez, O., Perrussel, O., Denier Van Der Gon, H. A., Dellaert, S. N. C., and Ciais, P.: Can we use atmospheric CO_2 measurements to verify emission trends reported by cities? Lessons from a six-year atmospheric inversion over Paris, Gases/Atmospheric Modelling and Data Analysis/Troposphere/Physics (physical properties and processes), https://doi.org/10.5194/egusphere-2023-401, 2023.

Liu, Z., Ciais, P., Deng, Z., Lei, R., Davis, S. J., Feng, S., Zheng, B., Cui, D., Dou, X., Zhu, B., Guo, R., Ke, P., Sun, T., Lu, C., He, P., Wang, Y., Yue, X., Wang, Y., Lei, Y., Zhou, H., Cai, Z., Wu, Y., Guo, R., Han, T., Xue, J., Boucher, O., Boucher, E., Chevallier, F., Tanaka, K., Wei, Y., Zhong, H., Kang, C., Zhang, N., Chen, B., Xi, F., Liu, M., Bréon, F.-M., Lu, Y., Zhang, Q., Guan, D., Gong, P., Kammen, D. M., He, K., and Schellnhuber, H. J.: Near-real-time monitoring of global CO_2 emissions reveals the effects of the COVID-19 pandemic, Nat Commun, 11, 5172, https://doi.org/10.1038/s41467-020-18922-7, 2020.

Lu, S., Wang, J., Wang, Y., and Yan, J.: Analysis on the variations of atmospheric CO_2 concentrations along the urban–rural gradients of Chinese cities based on the OCO-2 XCO_2 data, International Journal of Remote Sensing, 39, 4194–4213, https://doi.org/10.1080/01431161.2017.1415482, 2018.

MacDonald, C. G., Mastrogiacomo, J.-P., Laughner, J. L., Hedelius, J. K., Nassar, R., and Wunch, D.: Estimating enhancement ratios of nitrogen dioxide, carbon monoxide and carbon dioxide using satellite observations, Atmos. Chem. Phys., 23, 3493–3516, https://doi.org/10.5194/acp-23-3493-2023, 2023.

Makarova, M. V., Alberti, C., Ionov, D. V., Hase, F., Foka, S. C., Blumenstock, T., Warneke, T., Virolainen, Y. A., Kostsov, V. S., Frey, M., Poberovskii, A. V., Timofeyev, Y. M., Paramonova, N. N., Volkova, K. A., Zaitsev, N. A., Biryukov, E. Y., Osipov, S. I., Makarov, B. K., Polyakov, A. V., Ivakhov, V. M., Imhasin, H. Kh., and Mikhailov, E. F.: Emission Monitoring Mobile Experiment (EMME): an overview and first results of the St. Petersburg megacity campaign-2019, Gases/Remote Sensing/Instruments and Platforms, https://doi.org/10.5194/amt-2020-87, 2020.

Molina, L. T., Madronich, S., Gaffney, J. S., Apel, E., De Foy, B., Fast, J., Ferrare, R., Herndon, S., Jimenez, J. L., Lamb, B., Osornio-Vargas, A. R., Russell, P., Schauer, J. J., Stevens, P. S., Volkamer, R., and Zavala, M.: An overview of the MILAGRO 2006 Campaign: Mexico City emissions and their transport and transformation, Atmos. Chem. Phys., 10, 8697–8760, https://doi.org/10.5194/acp-10-8697-2010, 2010.

Molina, L. T. Introductory lecture: air quality in megacities. Faraday discussions, 226, 9-52, 2021.

Park, H., Jeong, S., Park, H., Labzovskii, L. D., and Bowman, K. W.: An assessment of emission characteristics of Northern Hemisphere cities using spaceborne observations of CO2, CO, and NO2, Remote Sensing of Environment, 254, 112246, https://doi.org/10.1016/j.rse.2020.112246, 2021.

Porras, S., González del Castillo, M.E., López, O., Arredondo, T., Rivera, O., Ramonet, M., Laurent, O., Grutter, M.: Diseño y despliegue de una red piloto para la medición de CO2 con un sistema de microsensores, UNAM internal report, 2023: http://www.epr.atmosfera.unam.mx/Microsensores-2022/documentos/4_Red_piloto_CO2.pdf (last accessed on May 20, 2024)

Plaza-Medina, E. F., Stremme, W., Bezanilla, A., Grutter, M., Schneider, M., Hase, F., and Blumenstock, T.: Ground-based remote sensing of O3 by high- and medium-resolution FTIR spectrometers over the Mexico City basin, Atmos. Meas. Tech., 10, 2703–2725, https://doi.org/10.5194/amt-10-2703-2017, 2017.

Pougatchev, N. S., Jones, N. B., Connor, B. J., Rinsland, C. P., Becker, E., Coffey, M. T., Connors, V. S., Demoulin, P., Dzhola, A. V., Fast, H., Grechko, E. I., Hannigan, J. W., Koike, M., Kondo, Y., Mahieu, E., Mankin, W. G., Mittermeier, R. L., Notholt, J., Reichle, H. G., Sen, B., Steele, L. P., Toon, G. C., Yurganov, L. N., Zander, R., and Zhao, Y.: Ground-based infrared solar spectroscopic measurements of carbon monoxide during 1994 Measurement of Air Pollution From Space flights, J. Geophys. Res., 103, 19317–19325, https://doi.org/10.1029/97JD02889, 1998.

Rinsland, C. P., Jones, N. B., Connor, B. J., Logan, J. A., Pougatchev, N. S., Goldman, A., Murcray, F. J., Stephen, T. M., Pine, A. S., Zander, R., Mahieu, E., and Demoulin, P.: Northern and southern hemisphere ground-based infrared spectroscopic measurements of tropospheric carbon monoxide and ethane, J. Geophys. Res., 103, 28197–28217, https://doi.org/10.1029/98JD02515, 1998.

Rißmann, M., Chen, J., Osterman, G., Zhao, X., Dietrich, F., Makowski, M., Hase, F., and Kiel, M.: Comparison of OCO-2 target observations to MUCCnet – is it possible to capture urban XCO2 gradients from space?, Atmos. Meas. Tech., 15, 6605–6623, https://doi.org/10.5194/amt-15-6605-2022, 2022.

Rivera Cárdenas, C., Guarín, C., Stremme, W., Friedrich, M. M., Bezanilla, A., Rivera Ramos, D., Mendoza-Rodríguez, C. A., Grutter, M., Blumenstock, T., and Hase, F.: Formaldehyde total column densities over Mexico City: comparison between multi-axis differential optical absorption spectroscopy and solar-absorption Fourier transform infrared measurements, Atmos. Meas. Tech., 14, 595–613, https://doi.org/10.5194/amt-14-595-2021, 2021.

Rodgers, C. D.: Inverse Methods for Atmospheric Sounding: Theory and Practice, WORLD SCIENTIFIC, https://doi.org/10.1142/3171, 2000.

Sha, M. K., De Mazière, M., Notholt, J., Blumenstock, T., Chen, H., Dehn, A., Griffith, D. W. T., Hase, F., Heikkinen, P., Hermans, C., Hoffmann, A., Huebner, M., Jones, N., Kivi, R., Langerock, B., Petri, C., Scolas, F., Tu, Q., and Weidmann, D.: Intercomparison of low- and high-resolution infrared spectrometers for ground-based solar remote sensing measurements of total column concentrations of CO2, CH4 and CO, Atmos. Meas. Tech., 13, 4791–4839, https://doi.org/10.5194/amt-13-4791-2020, 2020.

Silva, S. J., Arellano, A. F., and Worden, H. M.: Toward anthropogenic combustion emission constraints from space-based analysis of urban CO_2/CO sensitivity, Geophysical Research Letters, 40, 4971–4976, https://doi.org/10.1002/grl.50954, 2013.

Storey, M. A. and Price, O. F.: Prediction of air quality in Sydney, Australia as a function of forest fire load and weather using Bayesian statistics, PLoS ONE, 17, e0272774, https://doi.org/10.1371/journal.pone.0272774, 2022.

Stremme, W., Ortega, I., and Grutter, M.: Using ground-based solar and lunar infrared spectroscopy to study the diurnal trend of carbon monoxide in the Mexico City boundary layer, Atmos. Chem. Phys., 9, 8061–8078, https://doi.org/10.5194/acp-9-8061-2009, 2009.

Stremme, W., Grutter, M., Rivera, C., Bezanilla, A., Garcia, A. R., Ortega, I., George, M., Clerbaux, C., Coheur, P.-F., Hurtmans, D., Hannigan, J. W., and Coffey, M. T.: Top-down estimation of carbon monoxide emissions from the Mexico Megacity based on FTIR measurements from ground and space, Atmos. Chem. Phys., 13, 1357–1376, https://doi.org/10.5194/acp-13-1357-2013, 2013.

Su, T., Li, Z., and Kahn, R.: Relationships between the planetary boundary layer height and surface pollutants derived from lidar observations over China: regional pattern and influencing factors, Atmos. Chem. Phys., 18, 15921–15935, https://doi.org/10.5194/acp-18-15921-2018, 2018.

Sussmann, R. and Rettinger, M.: Can We Measure a COVID-19-Related Slowdown in Atmospheric CO2 Growth? Sensitivity of Total Carbon Column Observations, Remote Sensing, 12, 2387, https://doi.org/10.3390/rs12152387, 2020.

Toon, G., Blavier, J.-F., Washenfelder, R., Wunch, D., Keppel-Aleks, G., Wennberg, P., Connor, B., Sherlock, V., Griffith, D., Deutscher, N., and Notholt, J.: Total Column Carbon Observing Network (TCCON), in: Advances in Imaging, Advances in Imaging, Vancouver, journalAbbreviation: HISensE, JMA3, 2009.

Viatte, C., Lauvaux, T., Hedelius, J. K., Parker, H., Chen, J., Jones, T., Franklin, J. E., Deng, A. J., Gaudet, B., Verhulst, K., Duren, R., Wunch, D., Roehl, C., Dubey, M. K., Wofsy, S., and Wennberg, P. O.: Methane emissions from dairies in the Los Angeles Basin, Atmos. Chem. Phys., 17, 7509–7528, https://doi.org/10.5194/acp-17-7509-2017, 2017.

Vogel, F. R., Frey, M., Staufer, J., Hase, F., Broquet, G., Xueref-Remy, I., Chevallier, F., Ciais, P., Sha, M. K., Chelin, P., Jeseck, P., Janssen, C., Té, Y., Groß, J., Blumenstock, T., Tu, Q., and Orphal, J.: XCO_2 in an emission hot-spot region: the COCCON Paris campaign 2015, Atmos. Chem. Phys., 19, 3271–3285, https://doi.org/10.5194/acp-19-3271-2019, 2019.

Wang, H., Jiang, F., Wang, J., Ju, W., and Chen, J. M.: Terrestrial ecosystem carbon flux estimated using GOSAT and OCO-2 XCO_2 retrievals, Atmos. Chem. Phys., 19, 12067–12082, https://doi.org/10.5194/acp-19-12067-2019, 2019.

Wang, Y., Broquet, G., Bréon, F.-M., Lespinas, F., Buchwitz, M., Reuter, M., Meijer, Y., Loescher, A., Janssens-Maenhout, G., Zheng, B., and Ciais, P.: PMIF v1.0: assessing the potential of satellite observations to constrain CO2 emissions from large cities and point sources over the globe using synthetic data, Geosci. Model Dev., 13, 5813–5831, https://doi.org/10.5194/gmd-13-5813-2020, 2020.

Wu, D., Lin, J. C., Fasoli, B., Oda, T., Ye, X., Lauvaux, T., Yang, E. G., and Kort, E. A.: A Lagrangian approach towards extracting signals of urban CO2 emissions from satellite observations of atmospheric column CO2 (XCO2): X-Stochastic Time-Inverted Lagrangian Transport model ("X-STILT v1"), Geosci. Model Dev., 11, 4843–4871, https://doi.org/10.5194/gmd-11-4843-2018, 2018.

Wunch, D., Wennberg, P. O., Toon, G. C., Keppel-Aleks, G., and Yavin, Y. G.: Emissions of greenhouse gases from a North American megacity, Geophysical Research Letters, 36, 2009GL039825, https://doi.org/10.1029/2009GL039825, 2009.

Xu, Y., Lauvaux T., Grutter, M., Taquet, N., García-Reynoso, J.A., Laurent, O., Lopez, M., Lian, J., Lin, X., Stremme, W., Ramonet, M., Atmospheric CO2 dynamics over a mountain urban basin: a case study of the Mexico City metropolitan area, submitted.

Ye, X., Lauvaux, T., Kort, E. A., Oda, T., Feng, S., Lin, J. C., Yang, E., and Wu, D.: Constraining fossil fuel CO_2 emissions from urban area using OCO-2 observations of total column CO_2, Gases/Atmospheric Modelling/Troposphere/Physics (physical properties and processes), https://doi.org/10.5194/acp-2017-1022, 2017.

1215   You, Y., Byrne, B., Colebatch, O., Mittermeier, R. L., Vogel, F., and Strong, K.: Quantifying the Impact of
1216 the COVID-19 Pandemic Restrictions on CO, CO2, and CH4 in Downtown Toronto Using Open-Path Fourier
1217 Transform Spectroscopy, Atmosphere, 12, 848, https://doi.org/10.3390/atmos12070848, 2021.
1218   Zhang, Q., Boersma, K. F., Zhao, B., Eskes, H., Chen, C., Zheng, H., and Zhang, X.: Quantifying daily NO$_x$
1219 and CO$_2$ emissions from Wuhan using satellite observations from TROPOMI and OCO-2, Atmos. Chem. Phys.,
1220 23, 551–563, https://doi.org/10.5194/acp-23-551-2023, 2023.
1221   Zhao, X., Marshall, J., Hachinger, S., Gerbig, C., Frey, M., Hase, F., and Chen, J.: Analysis of total column
1222 CO2 and CH4 measurements in Berlin with WRF-GHG, Atmos. Chem. Phys., 19, 11279–11302,
1223 https://doi.org/10.5194/acp-19-11279-2019, 2019.
1224   Zhou, M., Ni, Q., Cai, Z., Langerock, B., Nan, W., Yang, Y., Che, K., Yang, D., Wang, T., Liu, Y., and
1225 Wang, P.: CO2 in Beijing and Xianghe Observed by Ground-Based FTIR Column Measurements and Validation
1226 to OCO-2/3 Satellite Observations, Remote Sensing, 14, 3769, https://doi.org/10.3390/rs14153769, 2022.